Patient-specific iPSC models of neural tube defects identify underlying deficiencies in neuroepithelial cell shape regulation and differentiation

Ioakeim Ampartzidis[1*], Elliott M Thompson[1], Yashica Gupta[1], Andrea Krstevski[1], Nicola Elvassore[2,3], Eirini Maniou[2,3], Paolo de Coppi[4-8], Gabriel L Galea[1,#]

1. Developmental Biology and Cancer, UCL GOS Institute of Child Health, London, UK

2. Department of Industrial Engineering, University of Padua, Padua, Italy

3. Veneto Institute of Molecular Medicine, Padua, Italy.

4. Stem Cells and Regenerative Medicine, UCL GOS Institute of Child Health, London, UK

5. Department of Development and Regeneration, Woman and Child and UZ Leuven Clinical Department of Obstetrics and Gynaecology, KU Leuven, Leuven, Belgium.

6. Specialist Neonatal and Paediatric Surgery, Great Ormond Street Hospital for Children NHS Foundation Trust, London, UK.

7. Medical and Surgical Department of the Fetus, Newborn and Infant, Ospedale Pediatrico Bambino Gesù, IRCCS, Rome, Italy.

8. NIHR Great Ormond Street Hospital Biomedical Research Centre, London, UK

Corresponding author: g.galea@ucl.ac.uk

* Current address = Department of Biochemistry, University of Cambridge, Hopkins Building, Tennis Court Road, Cambridge CB2 1QW, UK

Key words: Neural tube defects, apical constriction, iPSC, planar cell polarity

Abstract

Spina bifida and anencephaly are neural tube defects caused by failure of embryonic neural tube closure. Successful closure requires elongation and apical constriction of neuroepithelial cells. These critical behaviours have not been studied in human, patient-specific models. We characterise a human iPSC-derived neuroepithelial morphogenesis model which is highly reproducible between lines. Differentiated neuroepithelial cells actively undergo ROCK-dependent apical constriction. ROCK acts downstream of planar cell polarity/VANGL2 in other species. We find that VANGL2 is up-regulated and phosphorylated during iPSCs-to-neuroepithelial differentiation. The patient-identified *VANGL2-R353C* mutation does not alter its expression, localisation or phosphorylation, but reduces myosin-II phosphorylation and apical constriction relative to congenic control iPSCs. Non-congenic comparisons and forward genetic testing are also informative in this reproducible model. We compare lines reprogrammed from amniocytes of two patients with spina bifida, versus two controls. One patient-derived line forms a morphologically normal neuroepithelium, but fails to differentiate into neurons. The second fails to undergo apicobasal elongation, and harbours compound heterozygous mutations in the *MED24* gene previously implicated in neuroepithelial elongation in mice. Thus, iPSC-derived neuroepithelial modelling provides mechanistic insights into conserved cell behaviours, links genetically-impaired apical constriction with a human disease, and establishes patient-specific models which recapitulate failures of heterogenous neuroepithelial functions.

Introduction

Neural tube defects (NTDs), such as spina bifida and anencephaly, affect approximately 1:1,000 births globally[1]. These severe neurodevelopmental malformations are caused by abnormal morphogenesis of the neural tube during embryonic development. The most severe NTDs result from failure of the physical process of neural tube closure, which in humans is completed by approximately 30 days gestation[2,3]. Completion of this morphogenetic process during largely inaccessible stages of pregnancy has limited our ability to study it in humans. This challenge is compounded by the multigenic causation of NTDs, as well as interactions of both maternal and embryonic genetics with environmental factors[4-6]. Consequently, few patients receive an interpretable genetic diagnosis. Typically, patient-identified mutations have been functionally validated in transgenic animal models [5,7-9].

Mice and other vertebrates have been invaluable models for understanding the process of neural tube closure. Both mice and humans close their open neural tube regions – called neuropores – through progressive elevation of neural folds which meet at the dorsal midline and zipper along the body axis[2,10]. The progression of closure requires the action of different cell types, particularly the surface ectoderm (future epidermis) and neuroepithelium (future brain and spinal cord)[3]. These cells coordinate multiple behaviours within and between each other: neuroepithelial cells thicken along their apicobasal axis as they differentiate into a pseudostratified epithelium which undergoes interkinetic nuclear migration synchronised with cell cycle progression, superimposed on active apical constriction[11-17].

Neuroepithelial apical constriction is an evolutionarily conserved force-generating mechanism which contributes to neural tube closure in chordates including amphibians, birds and mammals[3]. It requires targeted localisation and phosphorylation of non-muscle myosin II in the cell's apical domain. Myosin binds filamentous (F-)actin, cross-linking filaments and generating contractile mechanical force through power strokes[18]. Neuroepithelial apical enrichment of F-actin and phosphorylation of myosin both require Rho-associated kinase (ROCK)[19], which is in turn apically localised at least in part by signalling through the non-canonical wingless homology (Wnt)/planar cell polarity (PCP)

75 pathway[20,21]. PCP components promote neuroepithelial apical constriction in *Xenopus*
76 frogs[22,23], chickens[24] and mice[15,20], but this pathway has been difficult to study in human
77 epithelial models due to lack of quantifiable readouts relevant to this pathway's
78 functions *in vivo*.

79 PCP was originally described in *Drosophila* as a regulator of polarised cell features such
80 as hair cell bristle orientation[25-27]. Pathway components were later shown to be
81 conserved in vertebrates and contribute to neural tube closure[28-31]. The core PCP
82 pathway involves signalling through asymmetric receptor complexes on adjacent cells,
83 pairing van Gogh-like (VANGL) and Cadherin EGF LAG seven-pass G-type receptor
84 (CELSR) proteins on one cell, with frizzled (FZD)/CELSR complexes on the adjacent
85 cell[32]. Both VANGL and FZD branches of this pathway are involved in neural tube
86 closure[33,34], although the roles of VANGL2 are best understood in mice. VANGL2 can be
87 activated through phosphorylation following binding of PCP Wnt ligands[35,36].

88 PCP signalling drives two functionally distinct processes in neuroepithelial cells
89 essential for mammalian NT closure: early convergent extension and later apical
90 constriction. Global genetic deletion of *Vangl2* precludes medial convergence and
91 rostro-caudal elongation necessary to initiate neural tube closure in mouse embryos[37],
92 although this effect may be partly mediated by the adjacent mesoderm[38]. At later
93 developmental stages, however, VANGL2 promotes cytoskeletal reorganisation
94 involving F-actin planar polarisation and phosphorylation of non-muscle myosin IIB,
95 likely by ROCK[20,39-41]. We previously reported that VANGL2-dependent enhancement of
96 apical constriction increases apical tension required to elevate the neural folds in the
97 spinal region of mice[20], and others have implicated it in apical constriction of the anterior
98 neuroepithelium[22].

99 Mutations in PCP genes including *VANGL2*[42-47] have been identified in patients who
100 have NTDs and damaging variants in actomyosin-related cytoskeletal regulation are
101 enriched in individuals with spina bifida[48]. However, it has been challenging to study the
102 regulation of apical constriction in human neuroepithelial cell models. A previous study
103 described elegant modelling of neural tube closure by differentiation of induced
104 pluripotent stem cells (iPSCs) on micropatterned surfaces[49]. That model's formation of

105 neuroepithelium enveloped within a larger cyst limits access to its apical surface for
106 functional measurements, such as inference of mechanical tension through laser
107 ablation assays. Similarly, previous studies have demonstrated that disruption of
108 actomyosin regulation dilates apical surfaces on the inside of human iPSC-derived
109 neuroepithelial spheres[50,51]. Several models have also been described which enable
110 studies into later stages of neuroepithelial function as they differentiate into neural
111 progenitors and then neurons[52-55]. While these neurogenesis models provide insights
112 into later differentiation, they do not capture cell behaviours crucial for neural tube
113 closure.

114 We previously characterised a minimal model of neuroepithelial morphogenesis in
115 which a monolayer of cuboidal iPSCs apicobasally elongate into a complex,
116 pseudostratified neuroepithelium with a planar morphology[17]. Importantly, this model
117 presents readily accessible neuroepithelial apical surfaces which are directly
118 comparable in size with those of mouse embryos[17]. Moreover, the same protocol can be
119 extended to differentiate neuroepithelial cells into cortical neurons[56]. This enables
120 sequential assessment of neuroepithelial functions relevant to generating mechanical
121 deformations which close the neural tube and their subsequent differentiation which
122 normally occurs after completion of closure. Here, we show that neuroepithelial
123 development in this model is reproducible, even when comparing non-congenic iPSC
124 lines. We validate use of the model to study PCP components including ROCK and
125 VANGL2, finding that a *VANGL2* point mutation previously identified in a patient[46]
126 diminishes neuroepithelial apical constriction. Extension of the model to two iPSC lines
127 derived from individuals who have spina bifida identifies line-specific deficiencies
128 potentially relevant to their malformation. Strikingly, all three NTD-relevant lines –
129 *VANGL2* point mutation and two patient-derived lines – present failures of distinct
130 neuroepithelial functions, recapitulating the heterogeneity of these conditions.

131 **Results**

132 **Lineage-specific marker expression precedes morphological changes during**
133 **iPSC to neuroepithelium differentiation**

134 Intra-line variability often limits the use of iPSCs to model multigenic diseases, such as
135 NTDs, in which congenic controls are often impractical. In contrast, neuroepithelial
136 differentiation through dual SMAD inhibition (Figure 1a)[17,56] is highly reproducible
137 between different iPSC lines. We illustrate this using three previously reported iPSC
138 lines from healthy individuals, selected to represent different origins and reprogramming
139 methods (Figure 1b). Line HO193b was reprogrammed from male (46XY) amniocytes
140 through microfluidic delivery of modified mRNA[57,58]. SFC086-03-01 was reprogrammed
141 from adult female (46XX) fibroblasts using non-integrating Sendai virus[17,59]. 802-30F
142 was from endothelial cells of a Hispanic female (46XX) reprogrammed through
143 StemRNA[60]. Despite their varied origins, all three undergo equivalent, temporally
144 predictable changes in epithelial morphology during neuroepithelial differentiation
145 (Figure 1a-h).

146 These cells begin their differentiation as an apicobasally polarised cuboidal monolayer
147 approximately 25 μm thick with large apical areas approximately 60 μm^2 ('day 2', Figure
148 1c-g). During differentiation, they double their apicobasal length into a pseudostratified
149 epithelium[17] approximately 55 μm thick, with small apical surfaces around 10 μm^2 ('day
150 8', Figure 1c-g). Apicobasal elongation increases total epithelial volume,
151 accommodating ongoing cell division[17], yet the volume of individual cells decreases
152 from 1,550 μm^3 at the start of differentiation to 500 μm^3 at the end (Figure 1h). This
153 reduction in total cell volume is partly due to a halving of nuclear volume
154 (Supplementary Figure 1).

155 Neuroepithelial apical size and apicobasal thickness – properties whose dynamic
156 control enables neural tube closure in vivo[20,24,61,62] – are indistinguishable between non-
157 congenic iPSC lines at each stage of differentiation analysed (Figure 1c-g). Equivalent
158 neuroepithelial thickness and apical areas are also obtained in cultures differentiated by
159 different investigators (Supplementary Figure 2). All lines show a non-linear
160 morphological evolution during differentiation: apical area and apicobasal thickness

161 remain similar between days 2 and 4 of differentiation, but then change rapidly to a
162 plateau by day 6 of differentiation (Figure 1e-g). In contrast, their expression of
163 pluripotency markers such as NANOG and OCT4 are rapidly lost between days 2 and 4
164 of differentiation (Figure 1i,j)[17]. The cadherin CDH1 is similarly down-regulated early
165 during differentiation, switching to expression of the neuroepithelial CDH2 from day 4 of
166 differentiation (Figure 1i). The neuroepithelial marker PAX6 is detectably expressed
167 from day 4 and its expression increases between day 4 and 8 (Figure 1i,k).

168 This suggests that cells' expression of molecular neuroepithelial markers precedes their
169 morphological changes in apicobasal elongation and reduction in apical size.

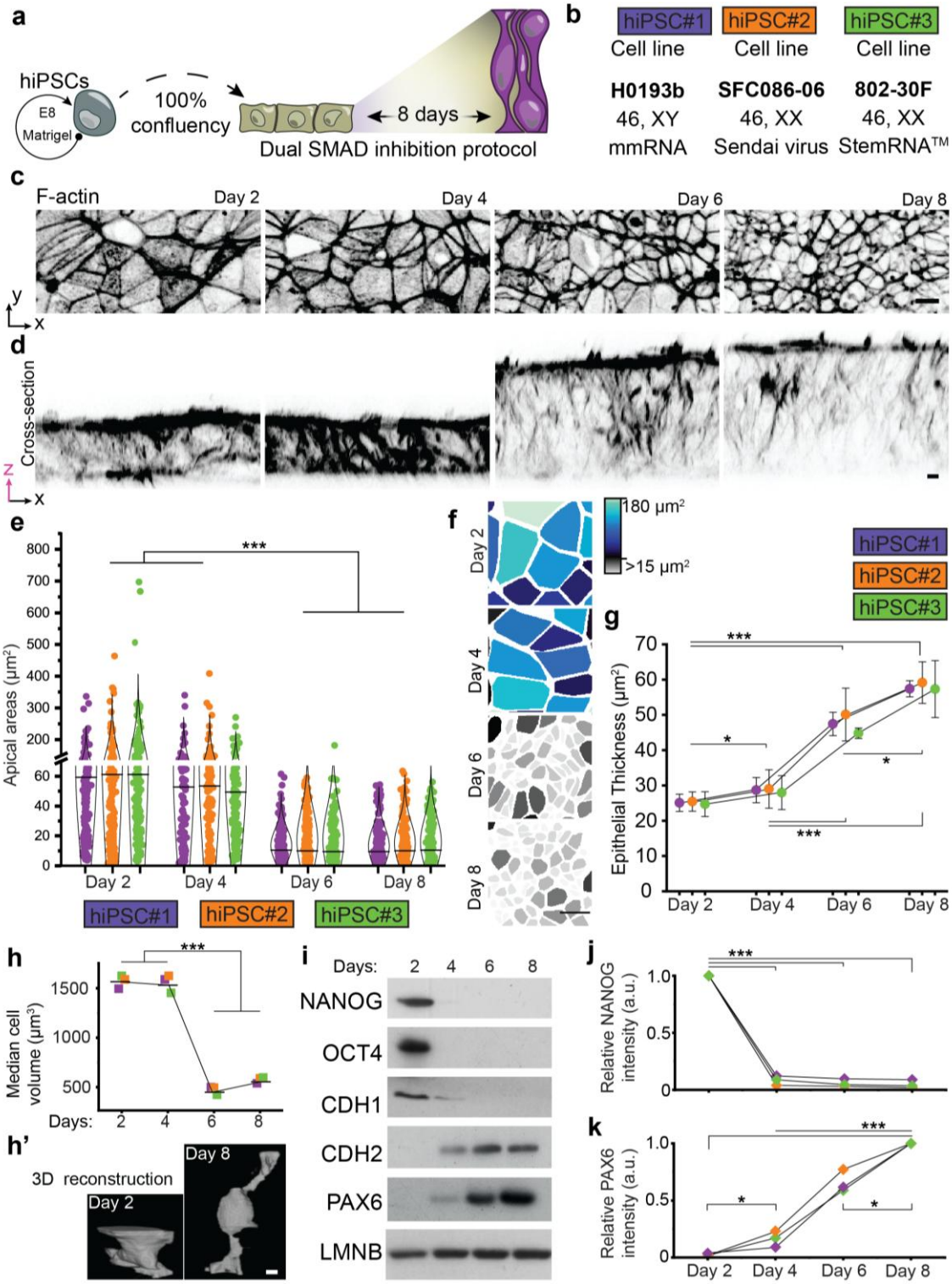

Figure 1: Reproducible morphological and molecular evolution of iPSC differentiation into neuroepithelial cells. iPSC1 is HO193b, iPSC2 is SFC086-03-01 and iPSC3 is 802-30F. ***a,*** *Schematic representation of the neuroepithelial induction protocol. Sub-confluent human iPSCs (in grey) are passaged and seeded at full confluency from the start of differentiation and*

175 *cultured for eight days, until reaching neuroepithelial maturity. Further passage at this stage*
176 *forms neural rosettes and allows further differentiation into post-mitotic neurons*[56]*.* ***b,*** *Summary*
177 *of control lines used to validate reproducibility of differentiation into neuroepithelial cells.* ***c,d,***
178 *Representative high-resolution confocal top-view (**c**) and cross-section (**d**) images of day 2-8*
179 *cultures fluorescently labelled to show F-actin with inverted gray LUT. P values from one-way*
180 *ANOVA with post-hoc Bonferroni.* ***e,*** *Dot plot representing cell's apical area across timepoints of*
181 *neuroepithelial differentiation, in three iPSC lines. Black bars represent the median apical area*
182 *across three culture plates of each line.* ***f,*** *Heatmaps of hiPSC2 representing the apical area*
183 *size changes during differentiation, in a contiguous area of 1,200 μm*^{2} *per timepoint.* ***g,***
184 *Quantification of epithelial thickness across neuroepithelial differentiation of control cell lines.*
185 *Three culture replicates were measured for each time point and cell line.* ***h,*** *Dot plot*
186 *representing the cell volume decrease across timepoints of differentiation, in control cell lines,*
187 *with representative 3D volumetric images at day 2 and day 8 (**h'**).* ***i,*** *Representative western blot*
188 *panel of NANOG, OCT4, CDH1, CDH2, PAX6, and LMNB protein levels across timepoints of*
189 *neuroepithelial differentiation, in the iPSC2 line. NANOG expression is normalised to day 2 per*
190 *line, whereas PAX6 is normalised to day 8 as it is not detected at day 2.* ***k,l,*** *Dot plots*
191 *representing normalised band intensity of NANOG (k), and PAX6 (l), across differentiation for*
192 *three control cell lines. Protein levels across all the cell lines were normalised to day 2. P values*
193 *from one-way ANOVA (**e,g**) or Wilcoxon paired test (**j,k**) with Bonferroni correction (***: p ≤*
194 *0.001, *: p ≤ 0.005). Scale bar = 10 μm.*

195

196 iPSC-derived neuroepithelial cells actively generate mechanical tension through 197 apical constriction

198 While reproducible between cultures, apical areas are variable within individual cultures
199 (Figure 1e): a hallmark of asynchronous apical constriction *in vivo*[63]. Through live
200 imaging, we observe that iPSC-derived neuroepithelial cells spontaneously and
201 dynamically alter their apical area (Figure 2a). Pharmacological inhibition of the myosin-
202 activating kinase ROCK increases neuroepithelial apical area (Figure 2b-c), as
203 previously observed in mouse embryos with equivalent ROCK inhibition *in vivo*[11].

204 The functional outcome of apical constriction is generation of mechanical tension which
205 is transmitted between adjacent cells and pulls on the surrounding tissue[20,64].
206 Contractile neuroepithelial apical tension can be inferred through annular laser ablation
207 assays[11,20], in which release of a small cluster of cells from their neighbours causes
208 rapid retraction of the cell borders within the ablated ring (Figure 2d). Their tension is

209 significantly diminished following a short period of ROCK inhibition (Figure 2e),
210 confirming that it is actively established through apical constriction.

211 *In vivo*, the Rho/ROCK/myosin pathway can be activated by PCP/VANGL2
212 signalling[20,24], and is well-established to promote apical constriction[20,22,65]. We observe
213 that VANGL2 and its binding partner scribbled (SCRIB) are expressed at low levels from
214 early stages of neuroepithelial differentiation and are significantly up-regulated by the
215 end of the differentiation period (Figure 2f,g). Both are co-localised on the cell's apical
216 cortex (Supplementary Figure 3). Serine-79/82/84 tri-phosphorylation of VANGL2 also
217 increases significantly during differentiation, with a particularly large up-regulation
218 between days 4 and 6 (Figure 2h), coinciding with the reduction in apical area (Figure
219 1e). Thus, iPSC-derived neuroepithelial cells express the cellular machinery required for
220 physiological control of apical constriction and actively establish apical tension *in vitro*.

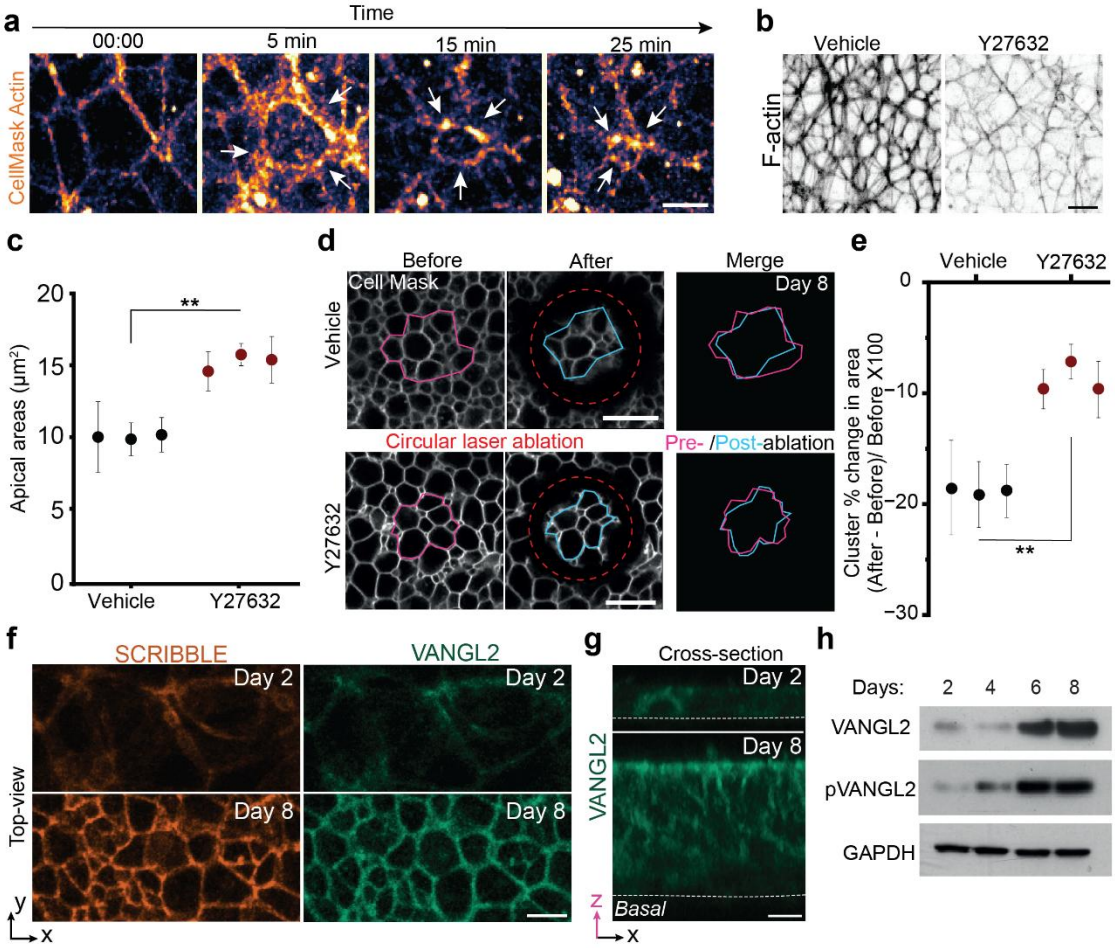

221

222 ***Figure 2: iPSC-derived neuroepithelial cells undergo ROCK-dependent apical***
223 ***constrictions and up-regulate expression of the PCP co-receptor VANGL2. a,*** *Live imaging*
224 *of day 8 neuroepithelial cultures stained with CellMask Actin dye.* ***b,*** *Representatives confocal*
225 *images of neuroepithelial cultures immunolabelled against ROCK1/2. Top view shows the*
226 *distribution of protein of interest across the apical areas and cross-section annotates protein*
227 *localisation along the apicobasal axis. Dashed line indicates the basal side.* ***c,*** *Representative*
228 *F-actin-stained images of cultures treated vehicle or 10 μM ROCK inhibitor (Y27632) for 4 hr.* ***d,***
229 *Dot plot representing the median apical area of day 8 SFC086 neuroepithelial cultures.* ***e,*** *Live-*
230 *imaged membrane-stained day 8 neuroepithelial cultures before and after a circular laser*
231 *ablation, shown in red dash line. Magenta and cyan outlined areas indicate the cell cluster recoil*
232 *before and after the ablation, respectively.* ***f,*** *Median apical cluster displacement of*
233 *neuroepithelial cells, across three independent replicates of. Each point represents the median*
234 *displacement quantified in each plate after at least three laser ablations.* ***g,h,*** *Representative*
235 *confocal images of SCRIB and VANGL2 immunolabelled cultures at day 2 and day 8, in of top-*
236 *view (**g**) and cross-section (**h**). Top view shows protein distribution across the apical areas and*
237 *cross-section annotates protein's localisation along the apicobasal axis. Dashed lines indicate*
238 *the basal side.* ***i,*** *Representative western blot panel of VANGL2, phosphorylated VANGL2*
239 *(pVANGL2), and GAPDH protein levels across timepoints of neuroepithelial differentiation, in*
240 *cell line. All analyses shown are in iPSC2. P values from Wilcoxon paired test with Bonferroni*
241 *correction (**: $p \leq 0.01$, *: $p \leq 0.005$). Scale bar = 10 μm.*

242

243 **An NTD-associated *VANGL2* mutation impairs neuroepithelial apical constriction**

244 To our knowledge, no genetic mutations identified in human patients have previously
245 been functionally associated with failure of apical constriction. The *VANGL2-R353C*
246 mutation (Figure 3a) was initially reported in a fetus which had both anencephaly and
247 spina bifida[46], and impairs other functions of PCP signalling in fruit flies[66]. This point
248 mutation causes a basic to polar amnio acid switch in a C-terminal region
249 (Supplementary Figure 4) which is highly conserved across species and mediates
250 interactions with pathway adaptor proteins[46,66]. We therefore considered it a high priority
251 target for testing in a human system.

252 We find that *VANGL2-R353C* mutation does not alter overall VANGL2 protein levels,
253 phosphorylation (Figure 3b,c), or apical localisation (Supplementary Figure 5) in two
254 iPSC clonal knock-in lines homozygous for this mutation compared with a congenic
255 control line. Knock-in and congenic control lines retain their ability to differentiate into
256 different germ layers (Supplementary Figure 6), achieve equivalent changes in
257 neuroepithelial apicobasal thickness (Supplementary Figure 7a-c) and nuclear
258 pseudostratification (Supplementary Figure 7d,e) during differentiation. The *VANGL2-*

259 *R353C* mutation does not significantly alter cell volume, nor does it diminish extension
260 of sub-apical protrusions which are characteristic of neuroepithelial cells[67]
261 (Supplementary Figure 8).

262 However, *VANGL2-R353C* knock-in lines have significantly larger apical areas (Figure
263 3d,e) and less apical localisation of phosphorylated myosin regulatory light chain
264 (Figure 3f,g) than their congenic controls. Laser ablation assays confirm that apical
265 tension is significantly lower in *VANGL2-R353C* knock-in lines than their congenic
266 controls (Figure 3h,i). Thus, this *VANGL2* mutation associated with human NTDs
267 selectively impairs neuroepithelial apical constriction.

268

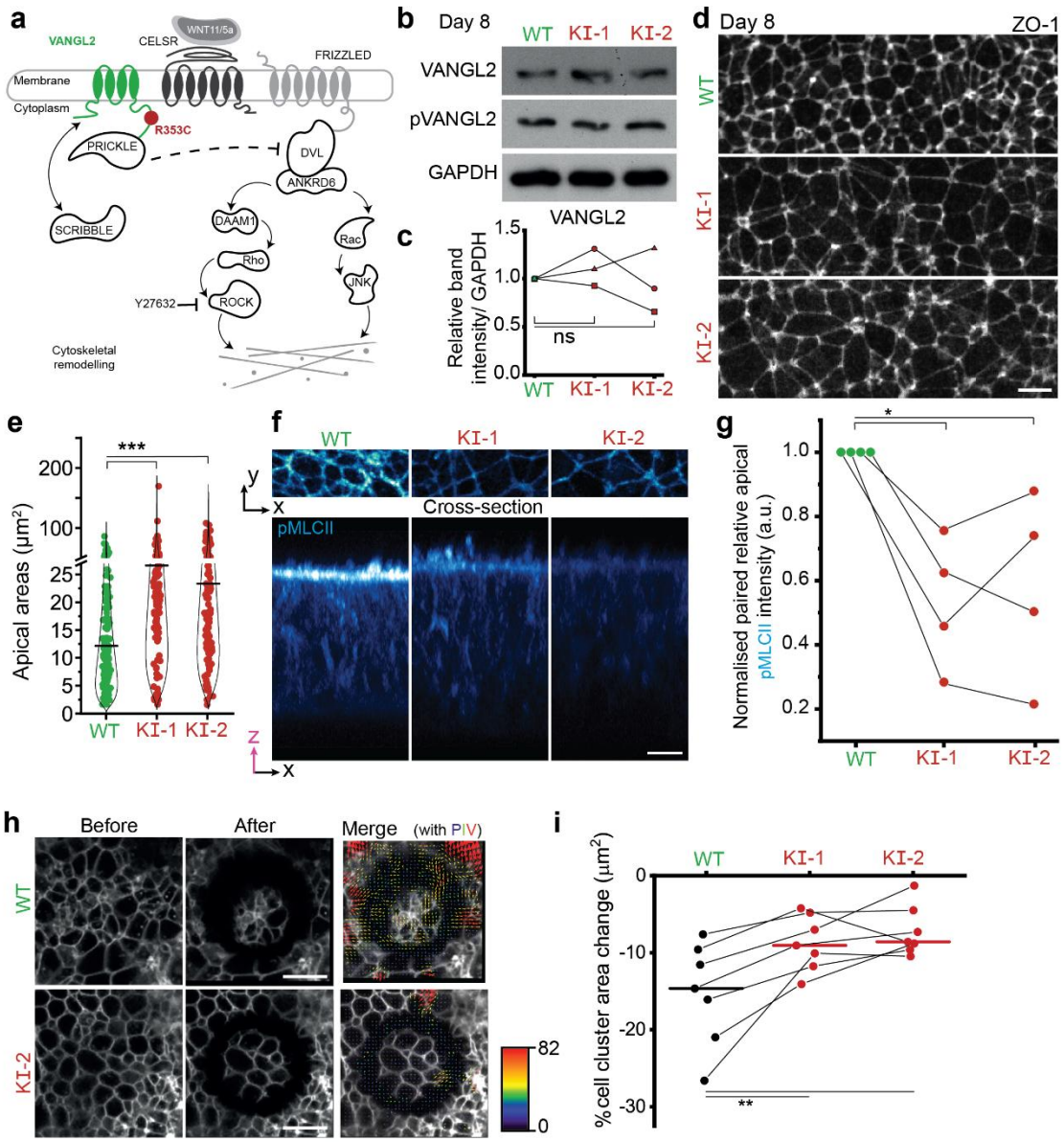

Figure 3: VANGL2-R353C mutation selectively impairs neuroepithelial apical constriction. ***a,*** *Schematic representation of PCP pathway, starting from non-canonical Wnt ligands (e.g. Wnt5a/11) interacting with membrane co-receptors and activating cytoskeletal remodeling responses. The transmembrane protein VANGL2 interacts with CELSR, which results to downstream interaction with cytoplasmic proteins such as PRICKLE and SCRIB. The VANGL2-R353C mutation is localised at the C-terminal region of the protein, in the prickle binding domain (Pk-D).* ***b,*** *Representative western blot against VANGL2 and pVANGL2 at day 8 of neuroepithelial differentiation in the isogenic control cell line (WT) and two knock in clones with the R353C mutation (KI-1 and KI-2).* ***c,*** *Dot plots representing VANGL2 and pVANGL2 relative band intensity levels after normalisation to GAPDH, respectively, across three replicates. Intensity levels across the three lines were normalised to the WT levels of each replicate.* ***d,*** *Representative high resolution confocal images of ZO-1 immunolabelled neuroepithelial cultures at day 8, across the WT and KI cell lines.* ***e,*** *Dot plot representing the median apical area size of day 8 neuroepithelial cultures, across the WT and KI cell lines. Lines link points from replicate cultures, with the WT intensity set at 1.* ***f,*** *Representatives confocal images of neuroepithelial*

cultures immunolabelled for phosphor-myosin light chain (pMLC)II, comparing the WT and KI-1 and KI-2 cell lines. Top view shows the distribution of protein of interest across the apical areas and cross-section illustrates localisation along the apicobasal axis. Scale bar = 10 µm. ***g,*** *Dot plot showing normalised paired relative apical area pMLCII intensity, across the WT and KI-1 and KI-2 cell lines, on day 8 of differentiation. Relative apical intensity was normalised to WT and set at 1, for each paired analysis, across four plates.* ***h,*** *Live-imaged membrane-stained neuroepithelial sheet before and after a circular laser ablation, with overlayed image of post-ablation timepoint and particle image velocimetry (PIV) analysis. The size and colour of arrows in PIV analysis represent the direction and magnitude of recoil. Scale = 20 µm.* ***i,*** *Median apical cluster displacement of neuroepithelial cells, across seven independent replicates. Each point represents three individual quantifications in each plate and connected lines indicate paired cultures. P values from Wilcoxon paired test with Bonferroni correction (***: $p \leq 0.001$, *: $p \leq 0.005$, n.s.: not significant).*

Establishment of patient-derived models of neuroepithelial dysfunction

As well as reverse genetic studies, an additional application of this highly reproducible model is patient-specific testing of key neuroepithelial behaviours (Figure 4a). Importantly, short-loop reprogramming of amniotic fluid stem cells with microfluidic delivery of modified mRNA[57] enables rapid generation of patient-specific models in the ~4 months between spina bifida diagnosis and birth. Having patient-specific models for functional genetic testing may be particularly useful to stratify post-natal management, particularly of individuals with non-isolated NTDs[68]. As proof of principle, we used short-loop reprogramming to compare two iPSC lines derived from amniotic fluid cells of individuals who do not have spina bifida (here called GOC1-2 for simplicity) with two lines of individuals treated at Great Ormond Street Hospital who underwent foetal surgery for spina bifida (GOSB1-2). All four lines express comparably high levels of the iPSC marker NANOG before differentiation, and differentiate to form endoderm, ectoderm and mesoderm (Supplementary Figure 6).

Both control lines and the first spina bifida line - GOSB1 - achieve indistinguishable apical areas and thicknesses (Figure 4b-e), further testament to the excellent reproducibility of this modelling system when comparing non-congenic lines. In contrast, the spina bifida line GOSB2 fails to apicobasally elongate as much as other lines and retains larger apical areas (Figure 4b-e). We consider this is unlikely to represent an apical constriction defect: laser ablation assays show comparable retraction in the GOSB2 line compared with the other lines tested (Supplementary Figure 9). The

320 epithelia they form include mitotic cells which are not apically-located, in contrast to all
321 other cells studied which are pseudostratified and localise their mitoses apically
322 (Supplementary Figure 10). Unlike all other lines tested, differentiated GOSB2 cultures
323 also show abnormally heterogenous expression of CDH2 while partially retaining lamin
324 A/C (Figure 4f) at the end of the standard differentiation protocol. Attempts to adapt the
325 protocol to 'rescue' this phenotype are beyond the scope of this study given the
326 excellent reproducibility of differentiation in the seven other lines presented here.

327 We performed whole exome sequencing of all four amniocyte-derived lines to identify
328 coding variants of potential clinical relevance in GOSB1 and GOSB2. Variants were
329 compared with a list of genes previously associated with NTDs in mice and/or humans
330 (Figure 4g, Supplementary Table 1).

331 GOSB1 harbours 851 variant loci within 747 genes (Supplementary Table 2; Figure 4h).
332 Of all genes with variants, 27 are NTD-associated, such as *ZEB2* (variant 2-144389425-
333 T-C) and *ZIC5* (13-99970996-G-T). None of the variants in NTD-associated genes are
334 predicted to have a high transcript impact and all are heterozygous.

335 GOSB2, which has a more severe neuroepithelial phenotype, has 1122 variant loci in
336 939 unique genes of which 43 are in NTD-associated genes (Figure 4h). In this line, six
337 NTD-associated genes harbour variants predicted to have a high impact on transcript
338 sequence: *CSNK2A1*, *FAM20C*, *LFNG*, *MED24* and *PCSK5*.

339 Of these, *CSNK2A1* (20- 503643-G-GCATATTT), *MED24* (17-40019203-C-CACAT) and
340 *PCSK5* (9-76175222-AAATGGAATGGAATGAAATGG-A) have gnomAD variant allele
341 frequencies <0.1. *MED24* (formerly called *TRAP100)* is of particular interest because its
342 deletion in mice results in a thin neuroepithelium which is not pseudostratified[69],
343 equivalent to our observations during GOSB2 differentiation. This gene is part of the
344 mediator complex involved in RNA polymerase II transcriptional co-activation. GOSB2
345 cells have compound heterozygous frameshift mutations in the same repetitive region of
346 the final exon of this gene. We additionally confirmed that the same *MED24* variants are
347 present in independent exome sequencing of amniocytes from which GOSB2 had been
348 derived (Supplementary Table 4). Both frameshifts are in the 3' untranslated region but
349 are predicted to alter RNA structure, causing loss of a multi-branch loop (Figure 4i), and

350 may therefore diminish binding of translation-regulating proteins. To test this, we
351 compared MED24 protein levels between GOSB2 iPSCs and three control lines, finding
352 reduced protein abundance compared to all three controls (Figure 4j,k). Although
353 genetic rescue experiments are beyond the scope of this study, particularly given the
354 likelihood of gene-gene interactions, equivalence of the cellular phenotype we observed
355 with a published mouse model and confirmation of reduced protein abundance suggest
356 the *MED24* variants in this line are pathogenic.

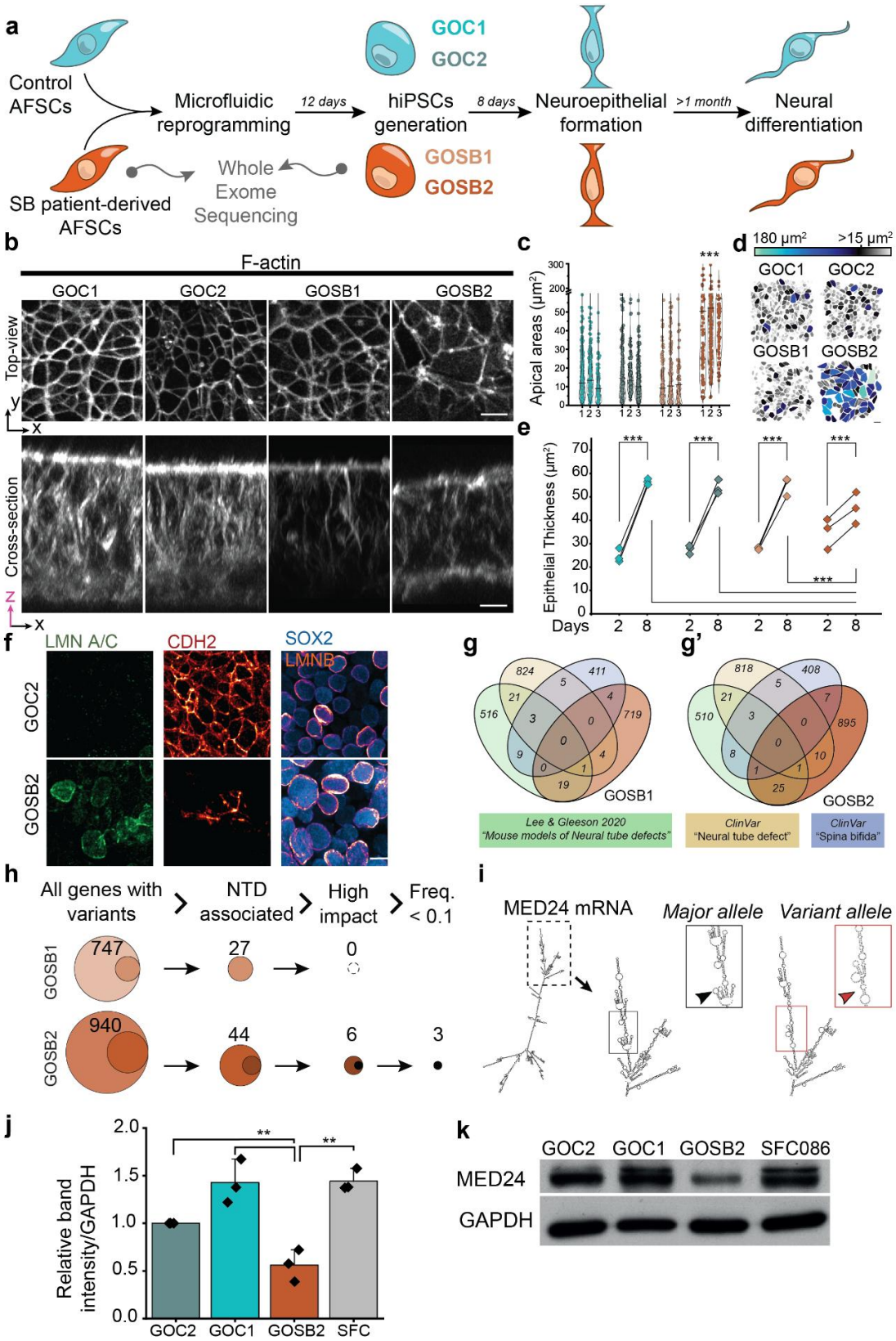

Figure 4: Spina bifida patient amniocyte-derived iPSC lines show can identify line-specific deficiencies in neuroepithelial cell function. a, *Experimental timeline of patient*

*amniocyte-derived iPSC lines**,** following microfluidic reprogramming. Whole exome sequencing was performed before and after reprogramming to identify line-specific deficiencies at genomic level and pair them to neuroepithelial and/or neural function level. **b,** Representative high-resolution top-view and cross-section images of day 8 neuroepithelial cultures visualizing F-actin. Two control cell lines (GOC1 and GOC2) were compared with two SB patient-derived hiPSCs cell lines (GOSB1 and GOSB2). **c,** Dot plot representing cell apical areas across the GOC1, GOC2, GOSB1, and GOSB2 cell lines at day 8 of neuroepithelial differentiation. Three independent plates were quantified for each line and the median apical area for each plate is shown with a black bar. **d,** Heatmaps representing the apical area size differences, across the four cell lines, in a contiguous area of 2,908 μm^2. **e,** Quantification of epithelial thickness on day 2 and day 8 samples, across four cell lines, GOC1, GOC2, GOSB1, and GOSB2. Points represent independent plate quantification for each line. Three paired replicates were measured for each time point and each cell line. Statistical test used for median values across quantifications was Wilcoxon paired test values with post-hoc Bonferroni **f,** Representative confocal images of LMN A/C, CDH2, SOX2, and LMNB immunolabelling in GOC2, and GOSB2, at day 8 neuroepithelial differentiation. **g,** Venn diagrams of GOSB1 and GOSB2 (**g'**) gene lists, after exome-sequencing, with at least one genetic variation observed in other datasets. Other datasets include previously associated mutations identified in humans under after search for the term "Neural Tube Defect" and "Spina Bifida" in ClinVar dataset, Lee and Geeson[5]. **h,** Filtering of variants in GOSB1 and GOSB2 to identify NTD-associated variants predicted to have a high impact on the transcript and which have a frequency <0.1 in gnomAD exome datasets. **i,** RNA structure of the MED24 major allele and rare variant (gnomAD reference 17-40019203-C-CACAT, allele exome frequency 0.018) predicted by RNAFold[70]. **j,** Bar plots representing normalised band intensity of MED24 across four cell lines. GOC2's intensity levels were set as 1 in each of three replicates. **k,** Western blot panel of iPSCs from four cell lines, GOC1, GOC2, GOSB2, and SFC086-06 showing MED24 protein and housekeeping GAPDH levels. Statistical test used for values was one-way ANOVA with post-hoc Bonferroni (***: $p \leq 0.001$, **: $p \leq 0.001$). Scale = 20 µm.*

As expected, given poor neuroepithelial morphogenesis of cells from the GOSB2 patient line, further differentiation does not produce polarised neural rosettes and results in only sparse differentiation of PAX6-positive neural progenitor cells with few neurites positive for the neuronal marker TUJ1 (Supplementary Figure 11). In contrast, GOSB1 formed prominent neuronal rosettes equivalently to the control lines (Figure 5a). However, by day 35 of neuronal differentiation, GOSB1 cultures show diminished TUJ1 positivity, without a change in the proportion of cells positive for the progenitor marker SOX2, compared with the two control lines differentiated in parallel (Figure 5b-d). Poor neuronal maturation in cells from the GOSB1 line is clearly evident by day 45 of differentiation, when control lines form dense aggregates interconnected by axons while GOSB1 cells form sparse and poorly-connected aggregates (Figure 5e,f). Thus, both the spina bifida patient-derived lines tested, in addition to *VANGL2-R353C* knock-in

model, demonstrate quantifiable yet distinct abnormalities in neuroepithelial functions (Figure 5g).

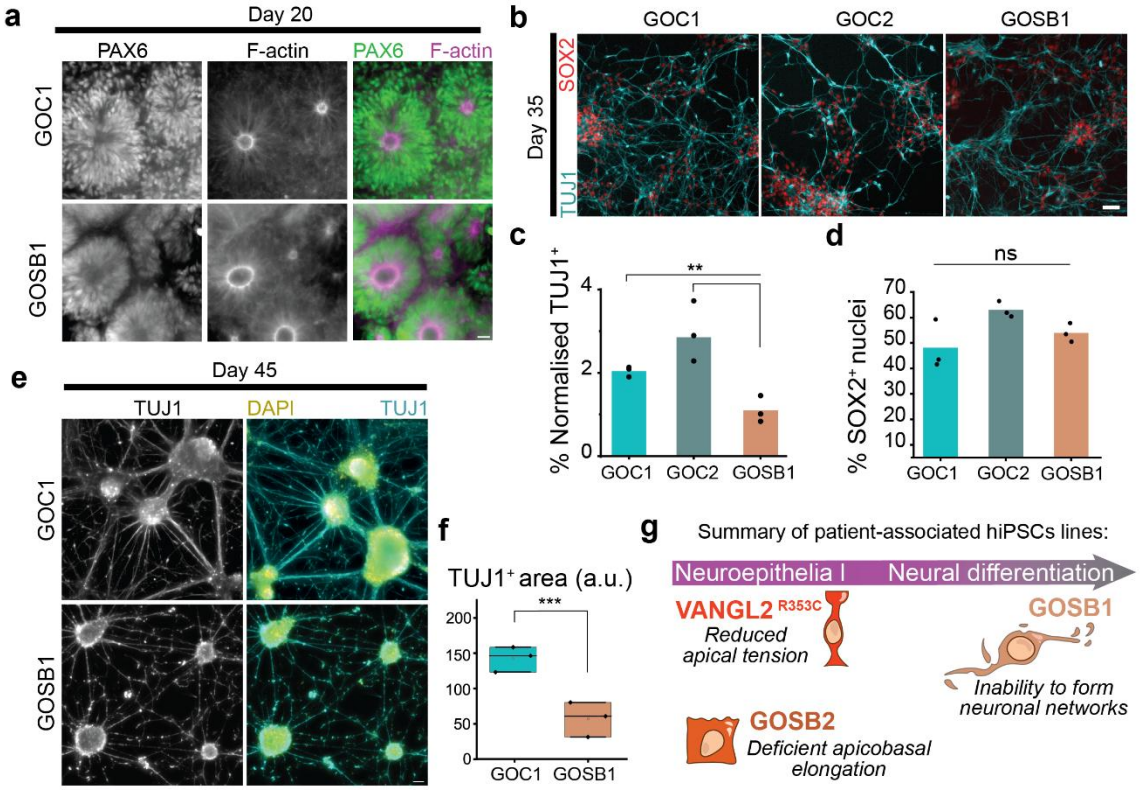

Figure 5: Diminished neuronal maturation suggests post-neurulation deficit of an iPSC lines derived from a patient with spina bifida. a, *Representative confocal images of GOC1, GOC2, and GOSB1 neuronal rosette cultures (day 20) immunolabelled against PAX6 and F-actin. Scale = 100 µm.* ***b,*** *Representative immunofluorescence panel of SOX2 and TUJ1 immunofluorescence of day 30 cultures, showing GOC1, GOC2, and GOSB1 lines. Scale = 50 µm.* ***c, d,*** *Dot plot representing the percentage of cells positive for TUJ1 (**c**) and SOX2 (**d**). Percentage positive nuclei were calculated in three independent replicates shown as an individual dots and the average is shown with the bars.* ***e,*** *Widefield images of day 45 GOC1 and GOSB1 neuronal cultures immunolabelled for TUJ1. Scale = 200 µm.* ***f,*** *Box plot representing the TUJ1 positive area quantified across three independent cultures of GOC1 and GOSB1 cell lines, on day 45 of differentiation. P values from one-way ANOVA with post-hoc Bonferroni (***: $p \leq 0.001$, **: $p \leq 0.001$, n.s.: not significant).* ***g,*** *Summary of patient-associated hiPSCs lines used in this study along with the stage of failure (red rhombi) to form a functional neuroepithelium or undergo mature neuronal formation in vitro.*

419 **Discussion**

420 We present a multifaceted yet tractable and reproducible model of neuroepithelial
421 morphogenesis which is sufficiently sensitive to identify NTD-associated dysfunctions in
422 both forward and reverse genetic studies. All three of the NTD-associated models we
423 compare – knock-in of a patient-identified *VANGL2* mutation and two patient-derived
424 iPSC lines – identify abnormalities which are specific to that line, and which are not
425 present in a panel of control lines tested. The abnormalities observed relate to apical
426 constriction, apicobasal elongation, and neuronal maturation.

427 Neuroepithelial apical constriction is required for closure of both the cranial and spinal
428 neural tube[11,14,15,21]. Mouse and *Xenopus* models establish VANGL2 as a conserved
429 enhancer of apical constriction[20,22,65] but, to our knowledge, this had never been shown
430 in a human system and no human genetic mutations have been linked to apical
431 constriction as a likely pathogenic mechanism. The mechanisms by which VANGL2
432 promotes apical localisation and activation of myosin[20] remain incompletely understood.
433 They may include both PCP-specific functions of *VANGL2* equivalent to those originally
434 identified for its orthologue in *Drosophila*, and potentially vertebrate-specific roles[71,72].
435 The neuroepithelial model presented here does not produce planar features commonly
436 used as characteristic readouts of PCP signalling *in vivo*[26,40]. Nonetheless, our
437 observation of increasing VANGL2 poly-phosphorylation suggests ligand-induced
438 pathway activation during differentiation[35]. This contrasts with decreasing VANGL2
439 phosphorylation previously reported during *in vitro* differentiation of lactogenic cells[71].

440 The diminished apical constriction phenotype we document following *VANGL2-R535C*
441 mutation occurs despite achieving wildtype-equivalent VANGL2 localisation, apicobasal
442 elongation and cell volume. These cellular phenotypes are consistent with previously-
443 reported mutations in the protein's C-terminus domain in mice[20,39,40]. VANGL2's C-
444 terminus contains the prickle-binding domain (directly affected by the R353C mutation)
445 and PDZ domain, which interacts with other components of the PCP pathway including
446 SCRIB[73]. SCRIB also enhances apical constriction[15,74].

447 We observe that apical constriction correlates with apicobasal epithelial thickening
448 during iPSC-to-neuroepithelial differentiation. This inter-relation is well-established in

449 *Drosophila* ventral furrow formation[75,76], and can be replicated following optogenetic
450 induction of apical constriction in cultured mouse cells[77]. However, we provide two lines
451 of evidence that this inter-relation during neuroepithelial differentiation is not simply due
452 to volume conservation, as had been suggested[76]. Firstly, cell volume decreases during
453 neuroepithelial differentiation as thickness increases. Secondly, neither epithelial
454 thickness nor cell volume are significantly altered in *VANGL2-R535C* neuroepithelial
455 cells with diminished apical tension. Mechanistic separability of apical constriction and
456 apicobasal elongation is consistent with biomechanical modelling of *Xenopus* neural
457 tube closure showing that both are independently required for tissue bending[61]. The
458 molecular regulation of neuroepithelial apicobasal elongation, and simultaneous
459 pseudostratification, has not been extensively studied. In *Xenopus,* microtubule-
460 regulating proteins are required for elongation[78], and in mice global deletion of *Med24*
461 results in a non-pseudostratified and thinner neuroepithelium[69]. Finding that a patient-
462 derived iPSC line with diminished MED24 expression fails to apicobasally elongate and
463 pseudo-stratify by the end of the standard differentiation period suggests this cell shape
464 change is also important in human neural tube closure.

465 Future work will be needed to determine whether *MED24* mutation is the only genetic
466 change relevant to neuroepithelial morphogenesis in GOSB2. Another limitation of our
467 model, shared by many *in vitro* systems, is the poor ability to replicate maternal
468 environmental influences. For example, the validated cell culture media used for this
469 model contain 3.4 mg/L folic acid instead of folate. This may mask NTD predispositions
470 caused by maternal folate deficiency or genetically impaired placental transport, while
471 accentuating cellular deficiencies which diminish folic acid conversion into a one-carbon
472 donor[79]. We cannot exclude *in vitro* accentuation of the cellular phenotype of the
473 GOSB2 line, as it is difficult to imagine that such severe failure of neuroepithelial
474 morphogenesis would produce a sufficiently normal spinal cord to benefit from fetal
475 surgery performed on the patient these cells were derived from. Alternatively,
476 compensation may be possible *in vivo*: for example, *Med1* knockout mouse embryos
477 also have thinned neuroepithelium but still achieve neural tube closure[80]. MED family
478 proteins are increasingly implicated in human neural tube defects: *MED12* and *MED13L*
479 likely pathogenic variants have been reported in patients[9,81]. Their functions during

480 neural tube closure, including through known interactions with Wnt and PCP
481 pathways[82], remain incompletely understood.

482 MED protein functions in neurogenesis and neuronal maturation are more well-
483 established[80,83-85]. Others previously reported that iPSC lines derived from individuals
484 who have spina bifida are less able to differentiate into neurons than those from healthy
485 controls[86]. This is consistent with our findings in the GOSB1 patient-derived line.
486 Although gene rescue experiments are beyond the scope of this study, potentially
487 deleterious variants identified in the GOSB1 patient line, including a *ZIC5* variant, may
488 impair neuronal development. The reduction in TUJ1 positive cells observed in this line
489 compared with non-congenic controls is at a point in differentiation which is highly
490 comparable between individuals and produces deep-layer cortical neurons[87]. Individuals
491 with spina bifida commonly have thinning of the neocortex and other supratentorial brain
492 abnormalities[88]. What is less clear is whether diminished neurogenesis, which normally
493 occurs after closure of the neural tube, may relate to causation of NTDs. The converse
494 – that open spina bifida impairs neural development – is directly supported by
495 experimental evidence[89]. Nonetheless, impaired neuronal differentiation of patient-
496 derived iPSC lines raises the potential for shared genetic/epigenetic causation of the
497 spinal lesion and cortical brain abnormalities, potentially compounded by abnormalities
498 in cerebrospinal fluid drainage and amniotic fluid exposure.

499 In summary, our findings in a human neuroepithelial model corroborate animal studies
500 identifying diminished apical constriction as a cause of NTDs, implicate VANGL2 acting
501 upstream of myosin phosphorylation in this behaviour, identify diminished
502 neuroepithelial thickness in a patient-specific disease model and corroborate the
503 importance of MED family proteins known to enhance this process as an emerging
504 genetic contributor to human NTDs. The highly reproducible modelling platform we
505 evaluate – which is robust to differences in iPSC reprogramming method, sex and
506 ethnicity – represents a valuable tool for future mechanistic insights and personalised
507 disease modelling applications.

508

Materials and Methods

Human iPSC culture maintenance

All iPSCs lines were grown in E8 medium (ThermoFisher, A1517001), using 0.5% Matrigel Growth Factor Reduced (Corning, 354277) coated plates, according to a previously published protocol (Beers et al., 2012). Cells were routinely grown in 6 well plates (SARSTEDT, 833920300), unless otherwise stated. E8 medium was fully replaced daily. At ~80% confluency cells were washed with PBS without $CaCl_2$/$MgCl_2$ (ThermoFisher,14190094) and dissociated with 0.5 mM EDTA (ThermoFisher, 15575020) for 5 min. Cells were resuspended in E8 medium and re-plated at a 1:10 split ratio. All cell lines were tested monthly for mycoplasma contamination, using the MycoAlert® kit (Lonza, LT07-318). A summary with the characteristics and reprogramming technologies of the hiPSCs lines used on this study can be found in Table 1.

Table 1: hiPSCs line information.

Cell line name	Designation#	Source	Karyotype	Reprogramming method
SFC086-03-01	iPSC2	Livesey Lab[17]	46, XX	Non-integrating Sendai virus
HO193b	iPSC1, GOC1	NIHR GOSH BRC*	46, XY	Microfluidic mmRNAs
HO471b	GOSB1	NIHR GOSH BRC*	46, XX	Microfluidic mmRNAs
HO220	GOC2	NIHR GOSH BRC*	46, XY	Microfluidic mmRNAs
HO541	GOSB2	NIHR GOSH BRC*	46, XY	Microfluidic mmRNAs
802-30F, parental	iPSC3, WT	SYNTHEGO	46, XX	StemRNA™ 3rd Gen
802-30F, VANGL2-R353C, clone E2	KI-1	SYNTHEGO	46, XX	StemRNA™ 3rd Gen
802-30F, VANGL2-R353C, clone F1	KI-2	SYNTHEGO	46, XX	StemRNA™ 3rd Gen

*# Shorthand nomenclature used in this paper for simplicity. *National Institute of Health Research Great Ormond Street Hospital Biomedical Research Centre*

527 **VANGL2 knock-in cell line generation**

528 The selection of the mutation was made according to a previously identified gene
529 alteration in a patient with craniorachischisis (Lei et al., 2010). The specific point
530 mutation was found in heterozygosity and was located on chromosome 1, at nucleotide
531 160,421,174 in the genomic sequence (Supplementary Figure 3). Although other *Vangl2*
532 mutations have been found to exert dominant negative effects[90], we generated
533 homozygous mutant lines to facilitate interpretation of results obtain. In collaboration
534 with SYNTHEGO, an established hiPSC line 802-30F was genetically engineered to
535 introduce a homozygous point mutation by replacing a cytosine (C) with a thymine (T)
536 (CGC>TGC), at a specific genetic locus. After high knock-in efficiency was confirmed,
537 specific sgRNA with Cas9 were electroporated to the cells. For the generation of the
538 isogenic control line (WT), the cells were electroporated with SpCas9 only and
539 confirmed to be unedited at target locus. Approximately two weeks later the cells
540 colonies have expanded and genotyping of the pool of clones was undertaken.
541 Individual clones were then isolated and clonally expanded to confirm the presence of
542 the knock-in genetic alteration. Those clones positive for the genetic alteration were
543 further Sanger sequenced to confirm stable *VANGL2* editing.

544

545 **Adherent neural induction protocol**

546 Direct differentiation of hiPSCs to neuroepithelial sheets was as we previously
547 reported[17]. Briefly, hPSCs were lifted with EDTA and plated at 100% confluency,
548 ~300,000 cells/cm^2, in E8 medium. It is critical to ensure that 100 % confluency is
549 reached at seeding (considered ‘day 1’). After 24 hours, cells were washed twice with
550 PBS without $CaCl_2$/$MgCl_2$ and the medium was replaced with 2 ml of neural
551 maintenance media (NMM, see Table 2), supplemented with 1 μM Dorsomorphin
552 (Tocris, 3093) and 10 μM SB431542 (Tocris, 1614). NMM with these supplements is
553 referred as neural induction medium (NIM) and was refreshed daily until day 8. At that
554 timepoint the cultures were terminated or passaged for neuronal differentiation.

Neuronal differentiation was performed as previously described[56]. The neuroepithelial sheets were passaged at day 8, using Dispase (ThermoFisher, 17105041) for 15-20 minutes at 37ºC. After washing with PBS, neuroepithelial clumps were plated on 1% Matrigel-coated 6-wells in NIM, ensuring sufficiently sparse seeding to give clumps space to form rosettes. After 24 hours of passaging, the medium was changed to NMM supplemented daily with 20 ng/ml of FGF2 (PeproTech, AF-100-18B) for the next four days. After day 12, neural rosettes were passaged to 1% Matrigel coated plates, using Dispase. NMM was then changed every 48 hours. This process was repeated at least three-times, when confluency reaches 80 %, until day 25 when the neural progenitor cells mature. At that stage, once the confluency reached 80 %, cells were passaged with Accutase (Sigma, A6964) to dissociate the rosettes into single cells. At that stage (~day 30) cells can be cryopreserved or plated for the last time at 25,000-75,000 cells/cm^2 on Laminin-521 (Gibco, A29249) coated plates.

Table Error! No text of specified style in document.**:** Composition of neural maintenance medium.

Product	Volume (ml)	Company	Cat. Number	Storage (ºC)
Solution A (500ml):				
2-Mercaptoethanol	1	Gibco	21985-023	4
DMEM/F12+Glutamax	481.25	Gibco	A15169-01	4
Insulin	0.25	Sigma	19278	4
N2 supplement (100x)	5	Gibco	17502-048	-20
Non-Essential amino Acids	5	Gibco	11140-050	4
Penicillin/Streptomycin	2.5	Gibco	15140-122	-20
Sodium Pyruvate	5	Sigma	S8636	4
Solution B (500ml):				
B27-supplement	10	Gibco	17504-044	-20
L-Glutamine	5	Gibco	25030-024	-20
Neurobasal	482.5	Gibco	12348-017	4
Penicillin/Streptomycin	2.5	Gibco	15140-122	-20

Immunofluorescent staining and confocal microscopy

Adherent cultures were stained for a maximum of 20 minutes in cold 4% paraformaldehyde (PFA) and immunofluorescent staining as previously described (Ampartzidis et al., 2023). Primary antibodies used were rabbit anti-ROCK (Abcam

575 antibody ab45171), rabbit anti-Ser19 pMLC (Cell Signalling Technology antibody
576 #3671), rabbit anti-SOX2 (Merck antibody ab5603), mouse anti-CDH2 (Cell Signaling
577 Technology antibody #14215), mouse anti-Lamin A/C (Santa Cruz antibody sc7292),
578 goat anti-Lamin B1 (Santa Cruz antibody sc6216), rabbit anti-ZO1 (Thermo Fisher
579 Scientific antibody #40–2200), goat anti-scribble (Santa Cruz antibody sc-11049), rat
580 anti-VANGL2 (Merck antibody, MABN750), rabbit anti-Pax6 (Biolegend antibody
581 901301), and mouse anti-TUJ1 (BioLegend MMS-435P), and detected with Alexa
582 Fluor™ conjugated secondary antibodies (Thermo Fisher Scientific). All primary and
583 secondary antibodies were used in 1:200 and 1:500 dilution, respectively. Nuclei were
584 labelled with DAPI (Severn Biotech Ltd 17057) and F-actin was labelled with Alexa
585 Fluor™-647 conjugated phalloidin (Thermo Fisher Scientific). Confocal salt and pepper
586 noise was removed using a 'remove outliers' filter and linear adjustments to brightness
587 and contrast were applied to parts of each figure panel equally.

588 Confocal images were captured on a Zeiss Examiner LSM880 confocal, using a
589 20x/NA1.0 Plan Apochromat dipping objective with AiryScan Fast. Widefield images of
590 the neural rosettes and neuronal cultures were captured on a Zeiss Observer inverted
591 using 10x/NA0.45 objective or a Nikon Ti2 Eclipse widefield microscope using
592 10x/NA0.30 or 20x/NA0.45 Plan Apochromat λD objectives.

593

594 **Laser ablations and live imaging**

595 Annual laser ablations were performed as previously reported[11,20] on day 8
596 neuroepithelial sheets. Briefly, cells were homogenously stained with CellMask
597 membrane dye (Invitrogen, C10046) and a single apical z-slice was selected for the
598 target region. The ablation circle was randomly placed in the stained neuroepithelial
599 sheet and three ablations were performed per dish then averaged (no predictable
600 change in tension was observed between repeated ablations in different fields of view).
601 The percentage reduction in cell area within the ablated annulus immediately after
602 ablation was quantified. The imaging order for each cell line was alternated between
603 each independent replicate to ensure no bias in the analysis and recoils were analysed
604 blinded to genotype/treatment.

605 For live-imaging sessions, day 8 neuroepithelial sheets were stained for 5 minutes with
606 CellMask Deep Red Actin Tracking stain (ThermoFisher, A57245) in NIM. Imaging was
607 performed with the Zeiss LSM880 confocal microscope using 20x/NA1.0 Plan
608 Apochromat dipping objective. The microscope chamber was pre-warmed at 37 ^{o}C and
609 CO_2 was set at 5 %. The water-immersive objective was cleaned with 70 % ethanol
610 solution and let to air dry to remove any potential contaminants. A plexiglass chamber
611 was assembled around the culture plate to maintain stable culture condition. Damp
612 cotton wool was put in the plexiglass set up to create a humidified chamber and avoid
613 media evaporation. ZEN Black v2.3 was used to operate the microscope and capture
614 images. Apical region images were acquired every 5 minutes.

615

616 **Particle intensity velocimetry (PIV) analysis**

617 Particle Image Velocimetry (PIV) examined the flow of apical areas of day 8
618 neuroepithelial sheets after laser ablations. Briefly, we identify changes in pixel flow
619 before and after the ablation. For the PIV analysis used in this report a pre-installed plug
620 in FIJI was used (Tseng et al., 2012). The analysis considers the displacement of pixels
621 within a specific region, termed 'interrogation window'. This area in the present study
622 was specified between two frames, before and immediately after the circular laser
623 ablation. For the analysis a 'Pure Denoise' filter (Cycle-spins: 4, Multiframe: 2) was used
624 to ensure that non-specific random noise is not interpreted as movement.

625

626 **Quantitative cell morphology analysis**

627 Apical area analyses were performed in F-actin stained neuroepithelial sheets, using
628 the polygon selection tool in FIJI and outlining the apical cap of individual cells and
629 saving them as ROIs. At least 100 contiguous cells were analysed from each image.

630 Epithelial apicobasal thickness, confocal images were optically resliced and their cross-
631 section outline manually annotated. Thickness was calculated using the 'bounding

632 rectangle' (width) tool in ImageJ/Fiji. This was performed in three images across each
633 dish and the average height was calculated for each culture.

634 For fluorescent signal polarisation analysis, the plot profile command in ImageJ/FIJI was
635 applied to an optically-resliced section of equal thickness within each dataset.

636

637 **TUJ1 and SOX2 neuronal quantification**

638 For the quantification of TUJ1+ axons of neural progenitor, the total area of axons was
639 quantified relative to the area imaged. The TUJ1 signal was binarized using the
640 'Threshold' command, and the total area of the axons was summed. Finally, the TUJ1+
641 area was normalised to the total number of cells per field of view.

642 For the quantification of SOX2 nuclear marker in neuronal progenitor cultures, a multi-
643 step pipeline was used. Initially, all nuclei were identified in the DAPI-stained channel
644 and using the command 'Find Maxima' in FIJI. A binarized image was generated, with
645 individual points within each nucleus. Each point was enlarged and used to generate a
646 ROI within each nucleus The individual points were used as a reference to quantify the
647 SOX2 intensity within each cell. A threshold was set manually after identifying the
648 nucleus with the lowest positive signal. Finally, the percentage for positive nuclei was
649 calculated after subtracting the total cell numbers with the positive proportion and
650 dividing by the overall cell number.

651

652 **Western blotting and quantification**

653 Western blotting was performed as previously described[91]. Neuroepithelial cells were
654 lysed on ice for 30 min in 50 mM Tris Base pH 7.6, 150 mM NaCL, 1% Triton X-100,
655 0.02% Sodium Azide, 1x protease inhibitor cocktail (Merck Life Science UK Ltd), 1 mM
656 sodium orthovanadate, 25 mM sodium fluoride. The protein concentration was
657 determined using Pierce BCA Protein Assay kits (Thermo Fisher). Proteins were
658 resolved by SDS-PAGE using 10-12% polyacrylamide gels and transferred to PVDF
659 membranes. Membranes were blocked in TBS (15.4 mM Trizma-HCL, 4.62 mM Tris-

660 base, 150 mM NaCl, pH 7.6) containing 10% w/v milk powder (Merck Life Science UK
661 Ltd). Membranes were incubated with primary antibody overnight and then with
662 horseradish peroxidase (HRP)-conjugated secondary antibodies (Agilent Technologies,
663 Stockport, UK) for 1 hour. Primary antibodies were used rabbit anti-pVangl2 (Merck
664 antibody SAB5701946), mouse anti-NANOG (Abcam antibody ab173368), rabbit anti-
665 OCT4 (Abcam antibody ab19857), mouse anti-CDH1 (R&D FAB18381A), mouse anti-
666 GAPDH (Merck antibody MAB374), rabbit anti-MED24 (BETHYL antibody A301-472A).
667 HRP was detected using ECL Prime (Cytiva, Amersham, UK). To strip and re-probe,
668 membranes were incubated in 0.2 M NaOH for 20 min at 37 °C and then 20 min at room
669 temperature before re-blocking and re-use.

670 For the quantification of western blot films, the band area method was applied using
671 ImageJ/FIJI. A box was drawn around the bands and after ensuring all bands fit within it,
672 and the intensity profile was plotted. The total area between the line graph and x axis,
673 after removing background, was quantified for each sample. The protein level was
674 normalised to the housekeeping protein, LMNB or GAPDH. The normalised protein
675 levels were compared between samples, and a control value was normalised to 1.
676 Protein quantifications were performed in paired replicates or in three independent cell
677 lines.

678

679 **Whole exome sequencing**

680 Approximately 500 ng of DNA from each cell line, namely GOC1, GOC2, GOSB1, and
681 GOSB2, were purified. The subsequent steps of fragmentation, library preparation,
682 Illumina sequencing were performed using established pipelines by Azenta, UK. Upon
683 receipt of the samples, a quality control (QC) screening was executed, and all samples
684 successfully pass the QC threshold including concentration and maintaining high DNA
685 integrity number (DIN, >7.8). FASTQ data QC, genomic alignment, variant colling and
686 annotation was also performed by Azenta, UK. For all samples, >97.5% of target
687 regions achieved a read depth ≥20X. Variants were annotated using the Sequence
688 Ontology consensus terms. The following were considered to have a high impact:
689 transcript_ablation (SO:0001893), splice_acceptor_variant (SO:0001574),

splice_donor_variant (SO:0001575), stop_gained (SO:0001587), frameshift_variant (SO:0001589), stop_lost (SO:0001578), start_lost (SO:0002012), and transcript_amplification (SO:0001889).

NTD associated gene sorting workflow

Lists of genes with annotated variants in GOSB1 and GOSB2 were compared with GOC1 and GOC2. Only variants not shared with GOC1/2 were considered in order to eliminate batch effects and very common variants. Each of resulting gene lists was then cross-referenced with the most current compilation of mouse models associated with NTDs, as documented in Lee and Gleeson[5]. Two additional gene lists were generated based on searches in ClinVar database for entries linked to "Neural Tube Defect" and "Spina Bifida" (Supplementary Table 1). Collectively, these identified a subset of variant genes associated with NTDs. These were subsequently filtered by sequency ontology severity score, and the allele frequencies of high impact variants was determined using gnomAD v4.1.0[92].

Statistical analysis and reproducibility

Comparisons between two groups were by Student's t-test accounting for homogeneity of variance in SPSS (IBM Statistics 25). Comparison of multiple groups was first tested for normality and homogeneity of variance in Origin 2020 (Origin Labs). According to the result if samples were normally distributed an ANOVA test was performed, while for non-parametric datasets a Kruskal-Wallis ANOVA was used in Origin 2020 (Origin Labs). Post-hoc pairwise analysis was performed to determine the statistical significance. P values <0.05 were considered statistically significant. All graphs were generated in Origin 2020. Replicates were defined as technical replicates (same iPSC line cultured at the same time) or biological replicates (different iPSC lines or same line cultured independently). In the case of VANGL2 knock-in lines, two clones were compared with their congenic control line. To avoid bias, blinding and randomisation was performed were possible by asking a lab member to rename copied files, without disclosing cell

line information prior to analysis. However, changes of neuroepithelial thickness across time points days was too dramatic to not know which day was analysed and morphological differences of GOSB3 also precluded blinding.

Acknowledgements

The authors would like to thank Prof F Livesey and Dr F Paonessa for their assistance in establishing the dual-SMAD inhibition protocol in our lab and provision of SFC086-03-01 as a reference line. We thank Jessica Reeves for technical assistance with western blots, Dr Teresa Pereira da Silva for scientific discussions and cell culture assistance, Dr Timo N. Kohler and Clara Munger for their critical reading of the manuscript, and Dr Dale Moulding for assistance with imaging. IA was funded by the NIHR GOSH Biomedical Research Centre. Views expressed in this manuscript are solely those of the authors and not necessarily those of the NHS, the NIHR or the Department of Health. GLG acknowledges funding from the Royal Society (RG\R2\232082), Rosetrees (2023\100266), NC3Rs (NC/Y50063X/1) and Wellcome Trust (211112/Z/18/Z).

Author contributions

IA, EMT, YG, AK and GLG performed and analysed experiments. GLG, PDC and NE conceived the study and designed experiments with IA. GLG, PDC and IA secured funding. GLG, PDC, NE and EM supervised staff. GLG and IA wrote the manuscript with input from all co-authors.

References

1 Zaganjor, I. *et al. PLoS One* **11**, e0151586, doi:10.1371/journal.pone.0151586 (2016).
2 Santos, C. *et al.* (eLife Sciences Publications, Ltd, 2024).
3 Nikolopoulou, E. *et al. Development* **144**, 552-566, doi:10.1242/dev.145904 (2017).
4 Chen, Z. *et al. Cell Res* **28**, 1039-1041, doi:10.1038/s41422-018-0061-3 (2018).
5 Lee, S. & Gleeson, J. G. *Trends Neurosci* **43**, 519-532, doi:10.1016/j.tins.2020.04.009 (2020).
6 Finnell, R. H. *et al. Front Genet* **12**, 659612, doi:10.3389/fgene.2021.659612 (2021).
7 Cao, X. *et al. Hum Mutat* **41**, 786-799, doi:10.1002/humu.23969 (2020).
8 Crane-Smith, Z. *et al. Hum Mol Genet* **32**, 2681-2692, doi:10.1093/hmg/ddad094 (2023).
9 Tian, T. *et al. Front Cell Dev Biol* **9**, 641831, doi:10.3389/fcell.2021.641831 (2021).
10 Maniou, E. *et al. Development* **150**, doi:10.1242/dev.202139 (2023).
11 Butler, M. B. *et al. J Cell Sci* **132**, doi:10.1242/jcs.230300 (2019).
12 McShane, S. G. *et al. Dev Biol* **404**, 113-124, doi:10.1016/j.ydbio.2015.06.003 (2015).
13 Ferreira, M. A. *et al. PLoS Comput Biol* **15**, e1007171, doi:10.1371/journal.pcbi.1007171 (2019).
14 Brooks, E. R. *et al. Elife* **9**, doi:10.7554/eLife.60234 (2020).
15 Lesko, A. C. *et al. Dev Biol* **478**, 59-75, doi:10.1016/j.ydbio.2021.05.013 (2021).
16 Smith, J. L. *et al. J Comp Neurol* **342**, 144-151, doi:10.1002/cne.903420113 (1994).
17 Ampartzidis, I. *et al. Dev Biol* **494**, 60-70, doi:10.1016/j.ydbio.2022.12.002 (2023).
18 Martin, A. C. & Goldstein, B. *Development* **141**, 1987-1998, doi:10.1242/dev.102228 (2014).
19 Escuin, S. *et al. J Cell Sci* **128**, 2468-2481, doi:10.1242/jcs.164574 (2015).
20 Galea, G. L. *et al. Nat Commun* **12**, 1159, doi:10.1038/s41467-021-21372-4 (2021).
21 McGreevy, E. M. *et al. Biol Open* **4**, 186-196, doi:10.1242/bio.20149589 (2015).
22 Kowalczyk, I. *et al. Development* **148**, doi:10.1242/dev.195008 (2021).
23 Ossipova, O. *et al. Nat Commun* **5**, 3734, doi:10.1038/ncomms4734 (2014).
24 Nishimura, T. *et al. Cell* **149**, 1084-1097, doi:10.1016/j.cell.2012.04.021 (2012).
25 Boutros, M. *et al. Cell* **94**, 109-118, doi:10.1016/s0092-8674(00)81226-x (1998).
26 Adler, P. N. *Bioessays* **14**, 735-741, doi:10.1002/bies.950141103 (1992).
27 Gubb, D. & Garcia-Bellido, A. *J Embryol Exp Morphol* **68**, 37-57 (1982).
28 Murdoch, J. N. *et al. Hum Mol Genet* **10**, 2593-2601, doi:10.1093/hmg/10.22.2593 (2001).
29 Kibar, Z. *et al. Nat Genet* **28**, 251-255, doi:10.1038/90081 (2001).
30 Wallingford, J. B. *et al. Nature* **405**, 81-85, doi:10.1038/35011077 (2000).
31 Rothbacher, U. *et al. Dev Biol* **170**, 717-721, doi:10.1006/dbio.1995.1249 (1995).

32 Aw, W. Y. & Devenport, D. *Curr Opin Cell Biol* **44**, 110-116, doi:10.1016/j.ceb.2016.08.002 (2017).
33 Yu, H. *et al. Development* **137**, 3707-3717, doi:10.1242/dev.052001 (2010).
34 Murdoch, J. N. *et al. Dis Model Mech* **7**, 1153-1163, doi:10.1242/dmm.016758 (2014).
35 Yang, W. *et al. Cell Res* **27**, 1466-1484, doi:10.1038/cr.2017.127 (2017).
36 Humphries, A. C. *et al. PLoS Genet* **19**, e1010849, doi:10.1371/journal.pgen.1010849 (2023).
37 Ybot-Gonzalez, P. *et al. Development* **134**, 789-799, doi:10.1242/dev.000380 (2007).
38 Nychyk, O. *et al. Dis Model Mech* **15**, doi:10.1242/dmm.049194 (2022).
39 Lopez-Escobar, B. *et al. Development* **145**, doi:10.1242/dev.157487 (2018).
40 Galea, G. L. *et al. Dis Model Mech* **11**, doi:10.1242/dmm.032219 (2018).
41 Baumholtz, A. I. *et al. Dev Biol* **428**, 25-38, doi:10.1016/j.ydbio.2017.05.013 (2017).
42 Doudney, K. *et al. Am J Med Genet A* **136**, 90-92, doi:10.1002/ajmg.a.30766 (2005).
43 De Marco, P. *et al. Birth Defects Res A Clin Mol Teratol* **100**, 633-641, doi:10.1002/bdra.23255 (2014).
44 Iliescu, A. *et al. Biochemistry* **53**, 5356-5364, doi:10.1021/bi500400g (2014).
45 Tian, T. *et al. Neurogenetics* **21**, 217-225, doi:10.1007/s10048-020-00613-6 (2020).
46 Lei, Y. P. *et al. N Engl J Med* **362**, 2232-2235, doi:10.1056/NEJMc0910820 (2010).
47 Kibar, Z. *et al. Clin Genet* **80**, 76-82, doi:10.1111/j.1399-0004.2010.01515.x (2011).
48 Aguiar-Pulido, V. *et al. Proc Natl Acad Sci U S A* **118**, doi:10.1073/pnas.2106844118 (2021).
49 Karzbrun, E. *et al. Nature* **599**, 268-272, doi:10.1038/s41586-021-04026-9 (2021).
50 Takla, T. N. *et al. Cells* **12**, doi:10.3390/cells12131697 (2023).
51 Tidball, A. M. *et al. Stem Cell Reports* **18**, 2498-2514, doi:10.1016/j.stemcr.2023.10.020 (2023).
52 Mirdass, C. *et al. Emerg Top Life Sci* **7**, 423-437, doi:10.1042/ETLS20230087 (2023).
53 Abdel Fattah, A. R. *et al. Cell Rep* **42**, 113334, doi:10.1016/j.celrep.2023.113334 (2023).
54 Krammer, T. *et al. Dev Cell* **59**, 1940-1953 e1910, doi:10.1016/j.devcel.2024.04.021 (2024).
55 Rabeling, A. *et al. Stem Cell Rev Rep* **20**, 2045-2061, doi:10.1007/s12015-024-10785-5 (2024).
56 Shi, Y. *et al. Nat Protoc* **7**, 1836-1846, doi:10.1038/nprot.2012.116 (2012).
57 Gagliano, O. *et al. Nat Protoc* **14**, 722-737, doi:10.1038/s41596-018-0108-4 (2019).
58 Maniou, E. *et al. Nat Mater* **23**, 1575-1581, doi:10.1038/s41563-024-01942-9 (2024).

59 Bluhmki, T. *et al. Methods Mol Biol* **1994**, 101-115, doi:10.1007/978-1-4939-9477-9_9 (2019).
60 Zhang, P. P. *et al. Acta Pharmacol Sin* **45**, 282-297, doi:10.1038/s41401-023-01172-w (2024).
61 Inoue, Y. *et al. Biomech Model Mechanobiol* **15**, 1733-1746, doi:10.1007/s10237-016-0794-1 (2016).
62 Schoenwolf, G. C. & Franks, M. V. *Dev Biol* **105**, 257-272, doi:10.1016/0012-1606(84)90284-7 (1984).
63 Matsuda, M. *et al. Nat Commun* **14**, 8475, doi:10.1038/s41467-023-43973-x (2023).
64 Campas, O. *et al. Nat Rev Mol Cell Biol* **25**, 252-269, doi:10.1038/s41580-023-00688-7 (2024).
65 Ossipova, O. *et al. Development* **142**, 99-107, doi:10.1242/dev.111161 (2015).
66 Humphries, A. C. *et al. Elife* **9**, doi:10.7554/eLife.53532 (2020).
67 Kasioulis, I. *et al. J Cell Sci* **135**, doi:10.1242/jcs.259897 (2022).
68 Che, X. *et al. Biology (Basel)* **11**, doi:10.3390/biology11091371 (2022).
69 Ito, M. *et al. EMBO J* **21**, 3464-3475, doi:10.1093/emboj/cdf348 (2002).
70 Hofacker, I. L. & Stadler, P. F. *Bioinformatics* **22**, 1172-1176, doi:10.1093/bioinformatics/btl023 (2006).
71 Rubio, S. *et al. Cells* **13**, doi:10.3390/cells13030222 (2024).
72 Walton, A. *et al. J Biol Chem* **300**, 106792, doi:10.1016/j.jbc.2024.106792 (2024).
73 How, J. Y. *et al. Biochem J* **478**, 1321-1332, doi:10.1042/BCJ20200816 (2021).
74 Boeda, B. *et al. J Cell Biol* **222**, doi:10.1083/jcb.202211113 (2023).
75 He, B. *et al. Nature* **508**, 392-396, doi:10.1038/nature13070 (2014).
76 Gelbart, M. A. *et al. Proc Natl Acad Sci U S A* **109**, 19298-19303, doi:10.1073/pnas.1205258109 (2012).
77 Martinez-Ara, G. *et al. Nat Commun* **13**, 5400, doi:10.1038/s41467-022-33115-0 (2022).
78 Suzuki, M. *et al. Development* **137**, 2329-2339, doi:10.1242/dev.048769 (2010).
79 Leung, K. Y. *et al. Brain* **136**, 2836-2841, doi:10.1093/brain/awt209 (2013).
80 Ito, M. *et al. Mol Cell* **5**, 683-693, doi:10.1016/s1097-2765(00)80247-6 (2000).
81 Ha, Y. J. *et al. Nature*, doi:10.1038/s41586-025-08676-x (2025).
82 Rocha, P. P. *et al. Development* **137**, 2723-2731, doi:10.1242/dev.053660 (2010).
83 Haque, F. *et al. Sci Adv* **8**, eadd1466, doi:10.1126/sciadv.add1466 (2022).
84 Hamada, N. *et al. Dev Neurosci* **43**, 43-52, doi:10.1159/000515188 (2021).
85 Zhu, W. *et al. Development* **142**, 465-476, doi:10.1242/dev.112946 (2015).
86 Sahakyan, V. *et al. Sci Rep* **8**, 2942, doi:10.1038/s41598-018-21103-8 (2018).
87 Strano, A. *et al. Cell Rep* **31**, 107732, doi:10.1016/j.celrep.2020.107732 (2020).
88 Fietz, S. A. *et al. J Neurosci* **40**, 1766-1777, doi:10.1523/JNEUROSCI.0192-19.2019 (2020).
89 Clark, M. *et al. bioRxiv*, 2025.2001.2006.631442, doi:10.1101/2025.01.06.631442 (2025).
90 Yin, H. *et al. PLoS One* **7**, e31988, doi:10.1371/journal.pone.0031988 (2012).
91 Thompson, E. M. *et al. FEBS Open Bio* **12**, 1388-1405, doi:10.1002/2211-5463.13418 (2022).
92 Chen, S. *et al. Nature* **625**, 92-100, doi:10.1038/s41586-023-06045-0 (2024).

880 **Supplementary Figures and Legends**

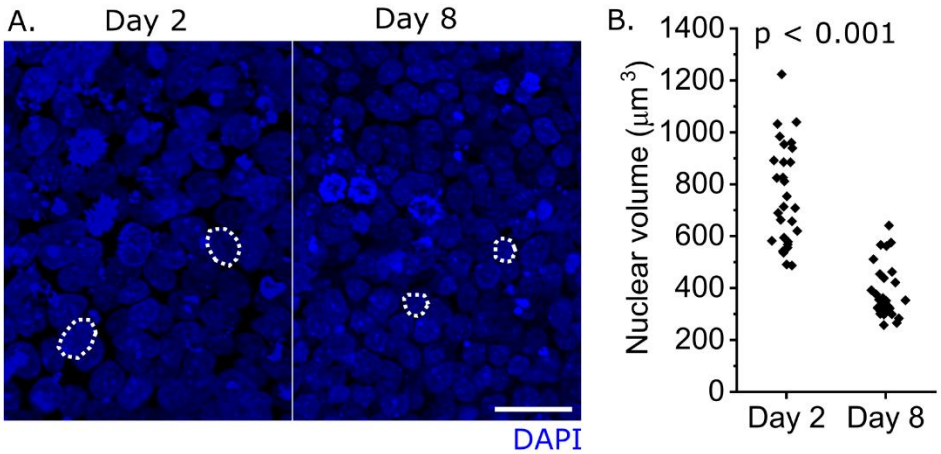

881

882 ***Supplementary Figure 1: Nuclear volume decreases during iPSC differentiation. a.***
883 *Visualisation of nuclei on day 2 and 8 of neuroepithelial differentiation. Dashed white lines*
884 *indicate nuclear outlines. Representative of multiple iPSC lines including iPSC1-3. Scale = 25*
885 *µm.* ***b,*** *Quantification of nuclear volume measured by manually drawing around each nucleus in*
886 *AiryScan Z-stacks spread throughout the apicobasal thickness of the epithelium. Points*
887 *represent individual nuclei (30 nuclei per day, 10 nuclei from three differentiation experiments).*

888

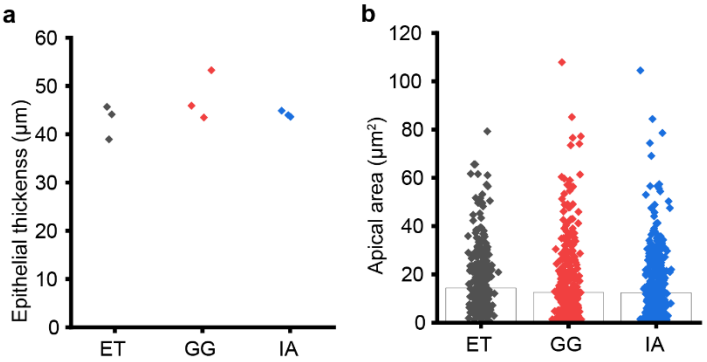

889

890 ***Supplementary Figure 2: Comparison of neuroepithelial morphology in cultures***
891 ***differentiated by three different investigators. a-b.*** *Neuroepithelial thickness (**a**) and apical*
892 *area (**b**) in iPSC2 cells differentiated by ET, GG and IA. All were analysed by GG. Points*
893 *represent different cultures (**a**) and individual cells (**b**, 300 cells from 3 cultures per investigator,*
894 *with bars showing medians). No groups are significantly different from others by T-test.*

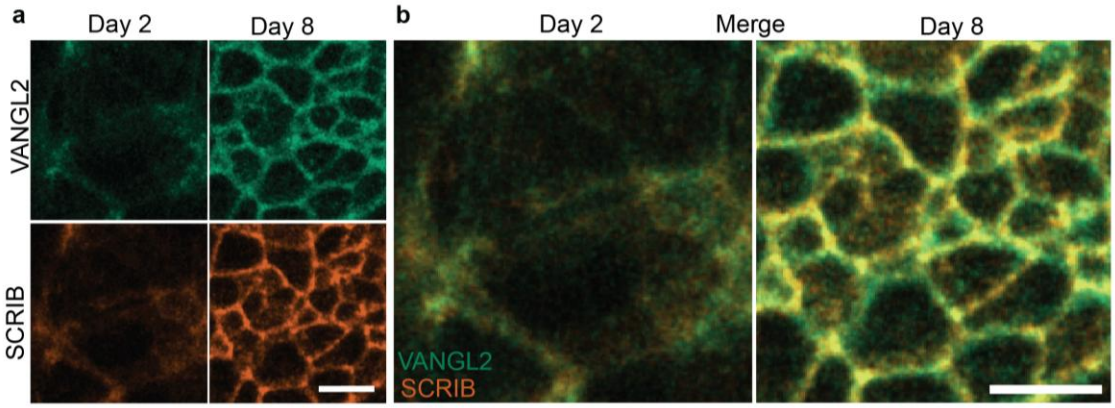

Supplementary Figure 3: SCRIB and VANGL2 co-immunolocalization in control hiPSCs. a. *Representative high-resolution max projection images of day 2 and day 8 neuroepithelial cultures stained against SCRIB, and VANGL2, in a control 802-30F line.* ***b.*** *Overlay of images showing co-immunolocalization of VANGL2 and SCRIB, on the cell cortex.*

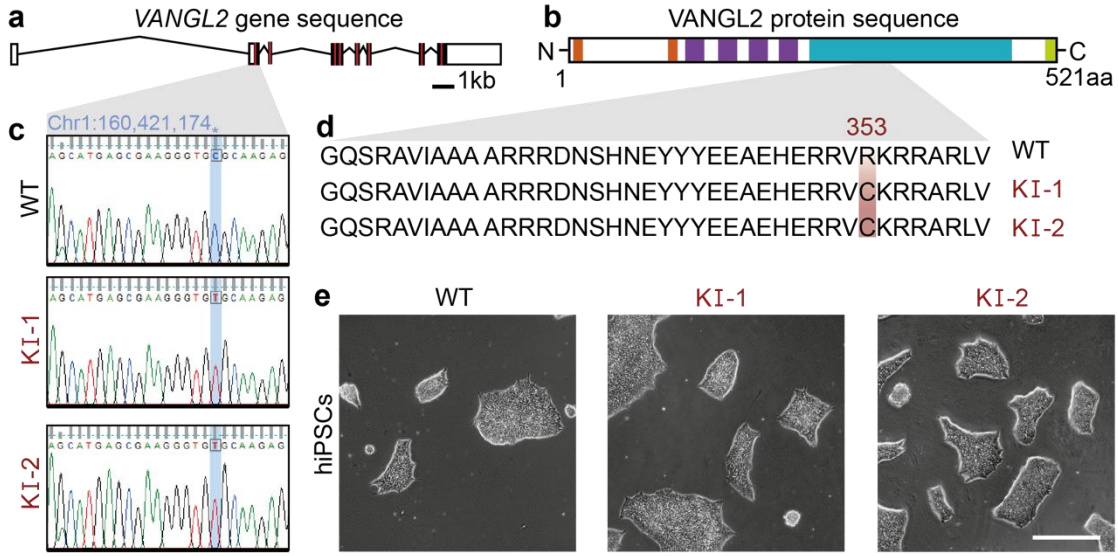

Supplementary Figure 4: Validation of knock-in mutation in hiPSCs clones and tri-lineage differentiation across all cell lines. a. *Human VANGL2 transcript sequence, according to Ensemble database (transcript ID: ENST00000368061.3). The coding regions are coloured in black, non-coding regions in white, and the red lines indicate previously identified mutated regions.* ***b.*** *Schematic representation of the structural organisation of VANGL2, of 521 amino acids (aa). Protein domains include: two Ser/Thr phosphorylation site clusters (orange), four transmembrane domains (purple), Prickle and Dishevelled protein interaction domain (cyan), and the C-terminal PDZ binding motif (PBM) domain (green).* ***c.*** *Sanger sequencing results for WT, F1, and E2 hiPSCs clones displaying a point mutation (C>T, highlighted in blue) at Chr1:160,421,174 locus. Reads for each of the four nucleic acids, A, T, C, G are annotated in green, red, blue, and black colours, respectively.* ***d.*** *VANGL2 protein sequence (312-360 aa) for each hiPSCs clone after the introduction of the point mutation. One amino acid replacement Arginine to a Cysteine (R>C) change was found at position 353 of the protein. E. Brightfield images of hiPSCs colonies from WT, F1, E2 hiPSCs clones, at passage 32. Scale = 500 µm.*

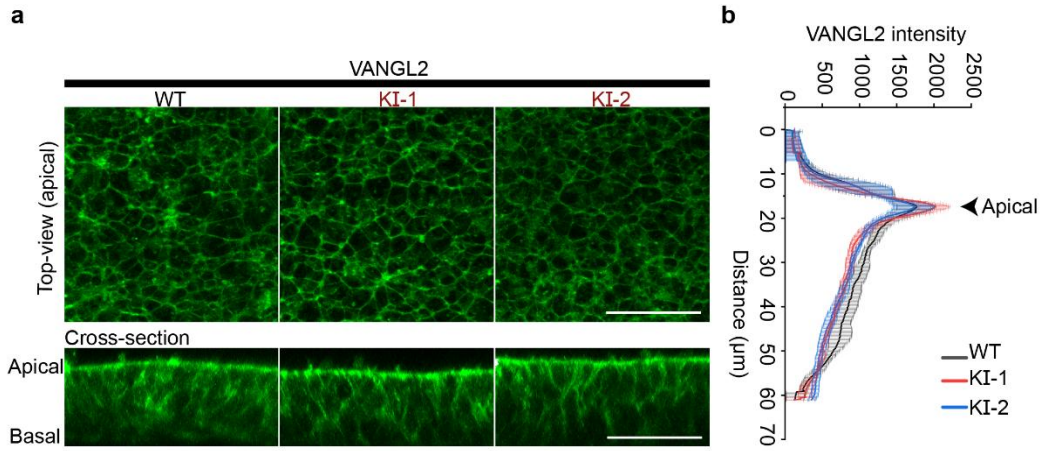

Supplementary Figure 5: VANGL2-R353C mutation does not alter apical localization. a. *VANGL2 immunofluorescence showing apical and lateral views of iPSC-derived neuroepithelium from the wildtype (WT) and two knock-in (KI) lines. Scale bar = 50 µm.* ***b.*** *Profile intensity quantification of VANGL2 immunofluorescence in three cultures of each line. Points represent the mean ± standard deviation. All plots are aligned so that their maximum values are in the same position.*

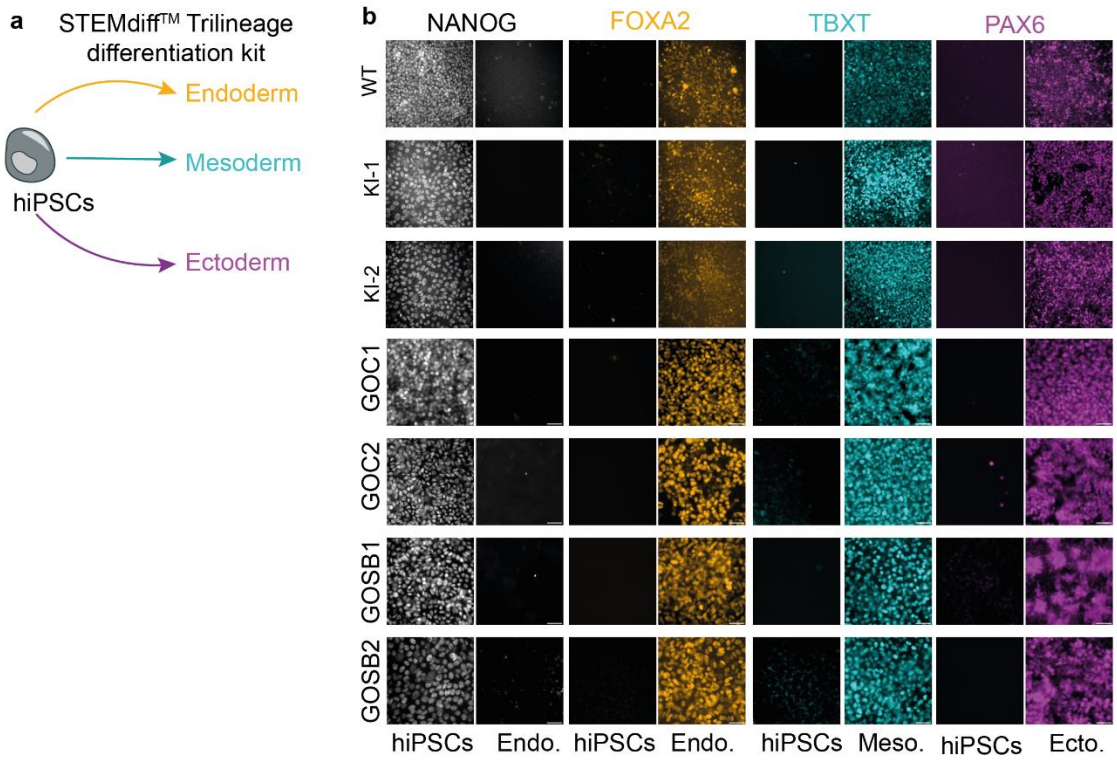

Supplementary Figure 6: Tri-lineage differentiation of hiPSC lines. *a. Schematic representation of tri-lineage differentiation protocol, using STEMdiff™ Trilineage Differentiation patient-derived cell lines after tri-lineage differentiation, with cells stained for NANOG (grey), FOXA2 (orange), T (cyan), and PAX6 (magenta) markers. Scale = 100 µm.*

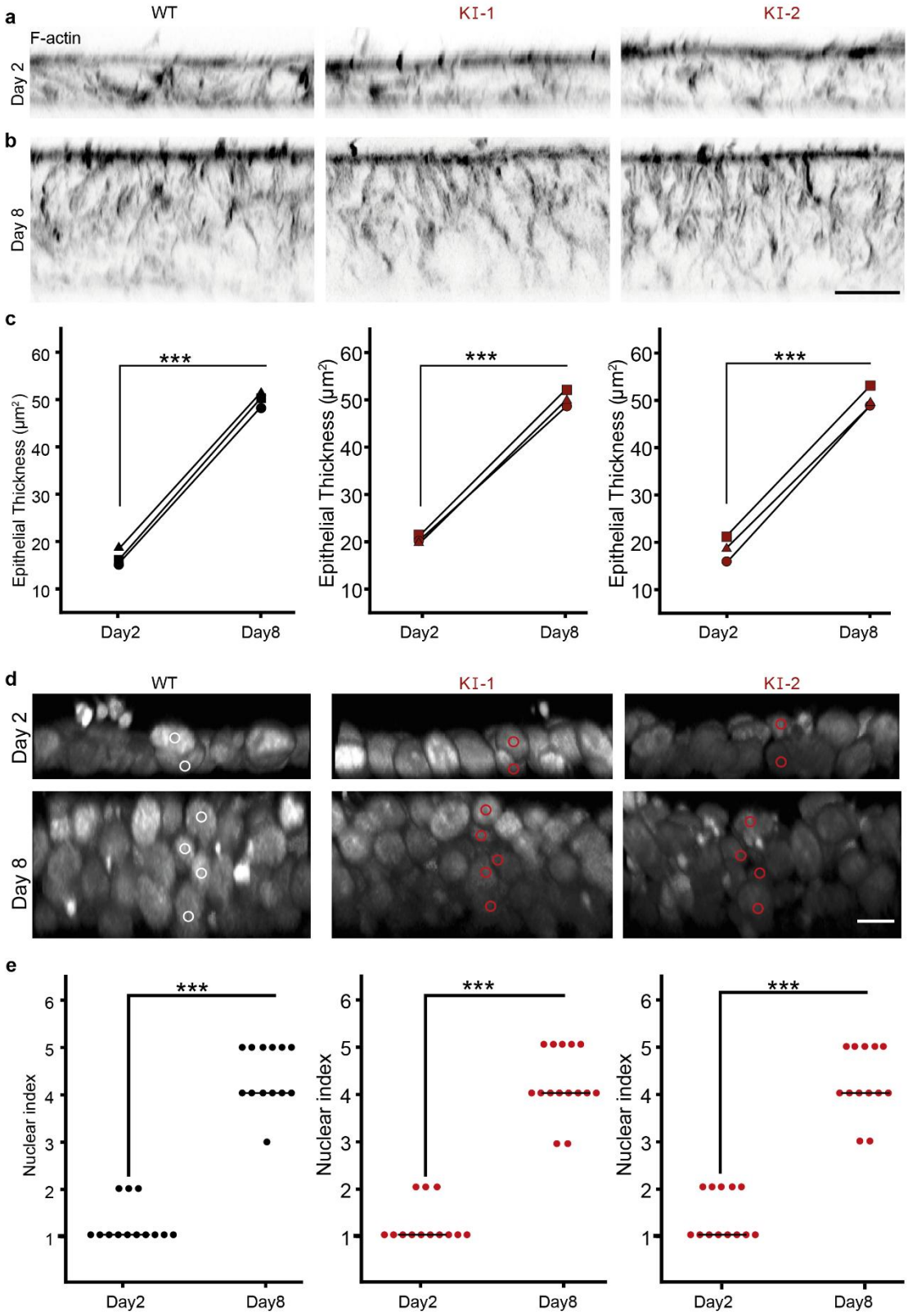
a
WT
KI-1
KI-2
F-actin
Day 2
b
Day 8
c
Epithelial Thickness (μm²)
***
Day2
Day8
d
e
Nuclear index

928

929 ***Supplementary Figure 7: VANGL2-R353C mutation does not impair neuroepithelial***
930 ***apicobasal elongation. a,b,*** *Optical cross-section of neuroepithelial sheets on day 2 (**a**) and*
931 *day 8 (**b**), after staining with F-actin (grey), respectively. Scale = 20 µm.* ***c,*** *Quantification of*
932 *epithelial thickness on day 2 and day 8 samples, across all cell lines. Points represent*
933 *independent plate quantification for each line. Three paired replicates were measured for each*
934 *time point and each cell line. Paired T-test was performed for mean epithelial thickness for each*
935 *cell line across day 2 and day 8 samples, and one-way ANOVA with post-hoc Bonferroni for the*
936 *day 8 comparison across the cell lines.* ***d, e.*** *Optical cross-section of neuroepithelial sheets on*
937 *day 2 (D) and day 8 (E), after staining with DAPI (grey). Dots annotate individual nuclei across*
938 *the epithelium. Scale = 20 µm.* ***f,*** *Quantification of nuclei dispersed in a row (nuclear index) of*
939 *day 2 and day 8 samples. Two sample T-test performed for mean nuclear index for each cell line*
940 *across day 2 and day 8 samples (***: p ≤ 0.0001, n.s.: not significant).*

941

942

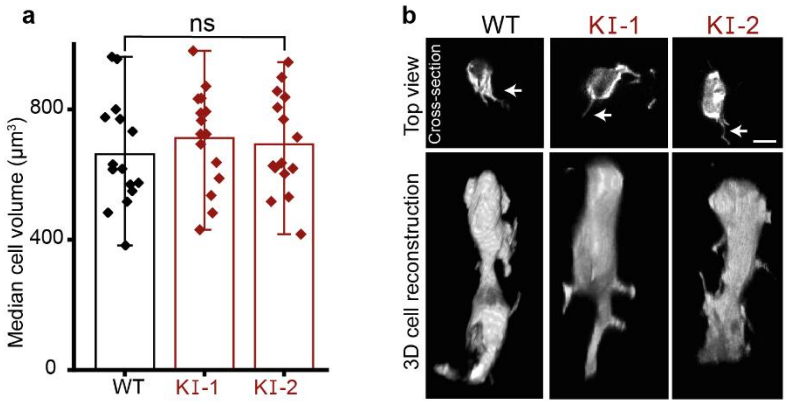

943

944 ***Supplementary Figure 8: VANGL2-R353C mutation does not alter neuroepithelial cell***
945 ***volume. a.*** *Bar graph overlaid with dot plot represent the quantification of neuroepithelial cell*
946 *volume across the WT, F1, and E2 cell lines, with 15 cells analysed in each cell line. Statistical*
947 *test used for individual cell volume and sub-apical protrusion length was Mann Whitney U-test*
948 *with post-hoc Bonferroni (n.s.: not significant).* ***b.*** *Representative image of subapical cross-*
949 *section of neuroepithelial cells stained for Bio-Tracker (grey). Arrowheads indicate sub-apical*
950 *protrusions. Scale = 20 µm.*

951

952

953

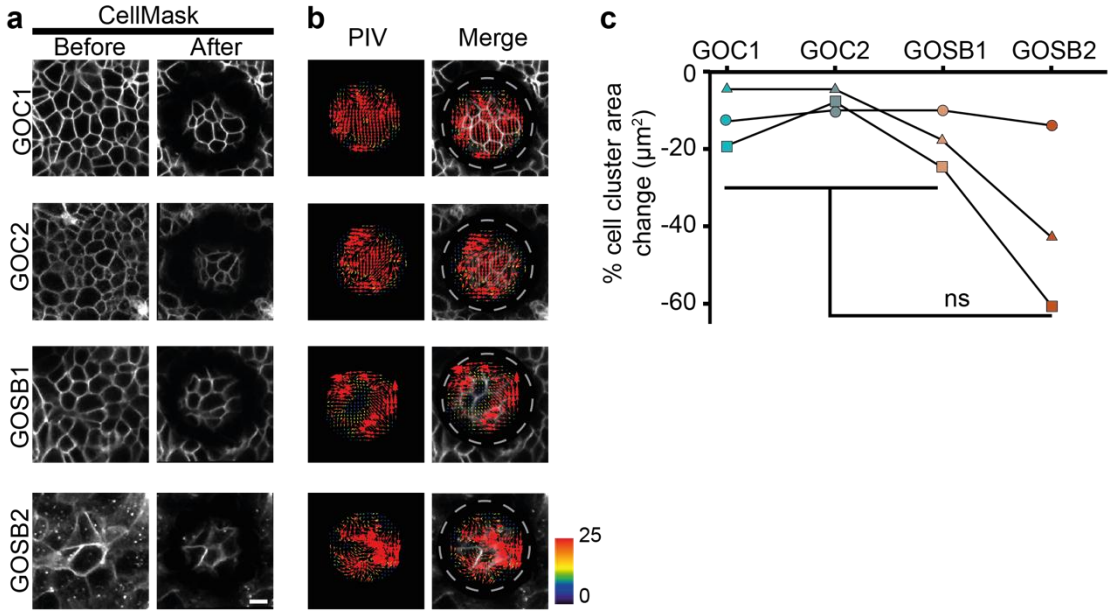

954

955 ***Supplementary Figure 9: Neuroepithelial cells differentiated from the control and spina***
956 ***bifida patient-derived iPSC lines show equivalent apical retraction following laser***
957 ***ablation. a.*** *Live-imaged CellMask-stained neuroepithelial sheet before and after a linear*
958 *circular laser ablation (white dash line). Scale = 20 µm.* ***b.*** *Particle image velocimetry (PIV)*
959 *analysis represent the direction recoil, in the last panel.* ***c.*** *Quantification of median apical*
960 *cluster displacement of neuroepithelial cells, across three independent biological plates.*
961 *Statistical test used for mean values across quantifications was one way ANOVA with post-hoc*
962 *Bonferroni (n.s.: not significant).*

963

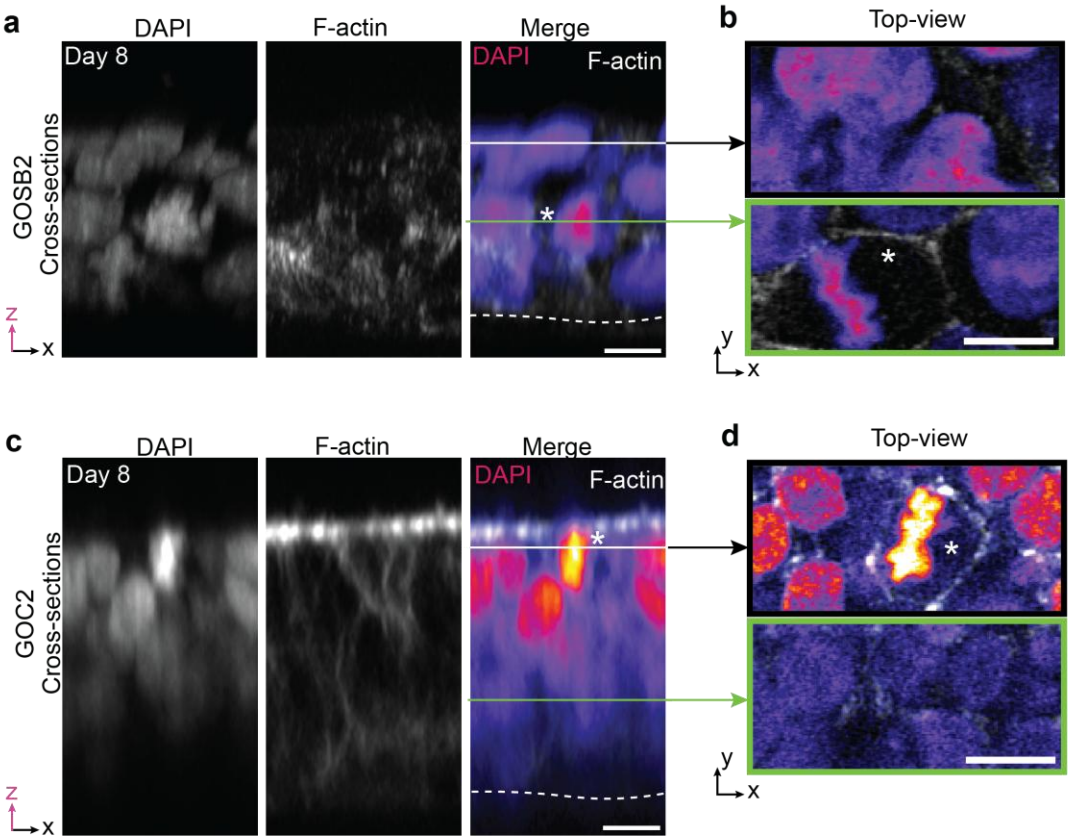

964

965 ***Supplementary Figure 10: Sub-apical localisation of mitotic figure in GOSB2 spina bifida***
966 ***patient-derived iPSC line. a,b.*** *Representative high-resolution confocal cross-section (A) and*
967 *top-view (B) images of day 8 GOSB2 cultures stained against F-actin and DAPI.* ***c, d.***
968 *Representative high-resolution confocal cross-section (**a**) and top-view (**b**) images of day 8*
969 *GOC2 cultures stained against F-actin and DAPI. Dashed lines indicate basal site of*
970 *neuroepithelial culture. The arrow lines (white and green) in both merged images correspond to*
971 *equivalent apical and basal slices shown in panel **b** and **d**, respectively for GOSB2 and GOC2.*
972 *Asterisk annotates the mitotic figure during metaphase.*

973

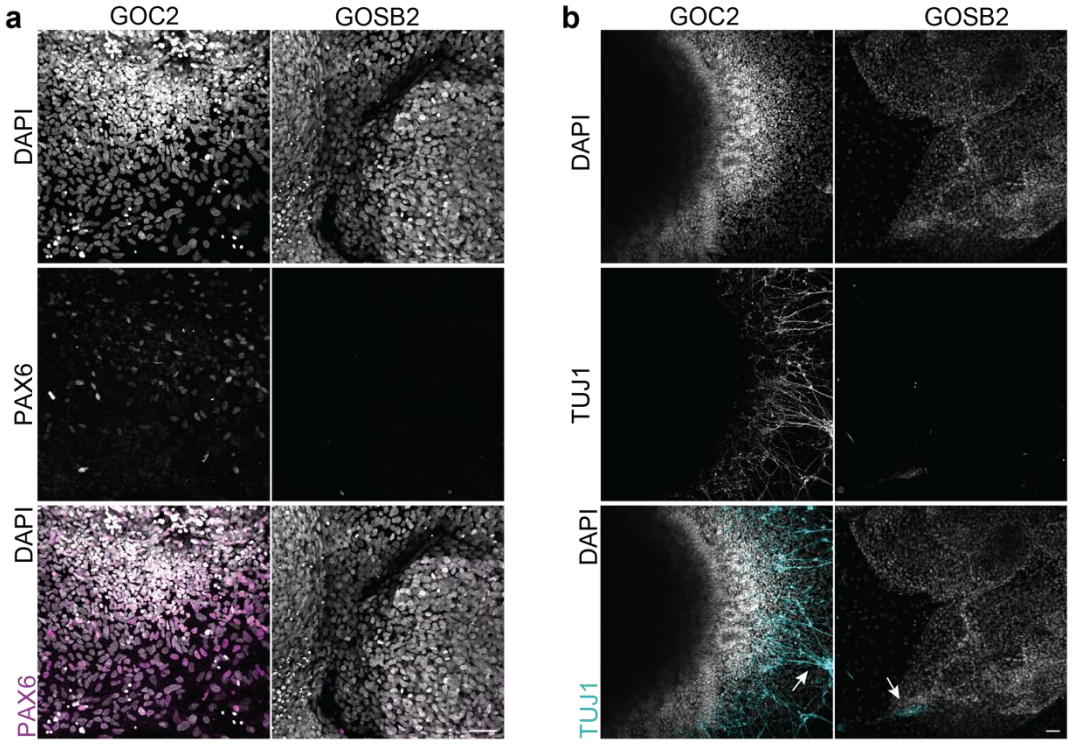

Supplementary Figure 11: Neuronal rosette characterisation between GOC2 and GOSB2 patient-derived cell lines. a. *Representative immunofluorescence panel of day 20, neuronal rosettes stage cultures stained against PAX6 (magenta) and DAPI (grey). Scale = 50 µm.* ***b.*** *Representative immunofluorescence panel of day 20, neuronal rosettes stage cultures stained against TUJ1 (cyan) and DAPI (grey). Arrows indicate TUJ1+ outgrowths. Scale = 50 µm.*